Stellar populations in the bulges of isolated galaxies

L. Morelli,[1,2]⋆ M. Parmiggiani,[1,2] E. M. Corsini,[1,2] L. Costantin,[1] E. Dalla Bontà,[1,2] J. Méndez-Abreu[3] and A. Pizzella[1,2]

[1] *Dipartimento di Fisica e Astronomia 'G. Galilei', Università di Padova, vicolo dell'Osservatorio 3, I-35122 Padova, Italy*
[2] *INAF – Osservatorio Astronomico di Padova, vicolo dell'Osservatorio 5, I-35122 Padova, Italy*
[3] *School of Physics and Astronomy, University of St. Andrews, SUPA, North Haugh, KY16 9SS St. Andrews, UK*

ABSTRACT

We present photometry and long-slit spectroscopy for 12 S0 and spiral galaxies selected from the Catalogue of Isolated Galaxies. The structural parameters of the sample galaxies are derived from the Sloan Digital Sky Survey *i*-band images by performing a two-dimensional photometric decomposition of the surface brightness distribution. This is assumed to be the sum of the contribution of a Sérsic bulge, an exponential disc, and a Ferrers bar characterized by elliptical and concentric isophotes with constant ellipticity and position angles. The rotation curves and velocity dispersion profiles of the stellar component are measured from the spectra obtained along the major axis of galaxies. The radial profiles of the Hβ, Mg and Fe line-strength indices are derived too. Correlations between the central values of the Mg$_2$ and $\langle$Fe$\rangle$ line-strength indices and the velocity dispersion are found. The mean age, total metallicity and total α/Fe enhancement of the stellar population in the centre and at the radius, where the bulge gives the same contribution to the total surface brightness as the remaining components, are obtained using stellar population models with variable element abundance ratios. We identify intermediate-age bulges with solar metallicity and old bulges with a large spread in metallicity. Most of the sample bulges display supersolar α/Fe enhancement, no gradient in age and negative gradients of metallicity and α/Fe enhancement. These findings support a formation scenario via dissipative collapse where environmental effects are remarkably less important than in the assembly of bulges of galaxies in groups and clusters.

Key words: galaxies: abundances – galaxies: bulges – galaxies: formation – galaxies: kinematics and dynamics – galaxies: spiral – galaxies: stellar content.

1 INTRODUCTION

Stellar populations are powerful diagnostics to constrain the assembly history of galaxy bulges. In the current picture, dissipative collapse (e.g. Gilmore & Wyse 1998), merging and acquisition events (e.g. Cole et al. 2000), and secular evolution (e.g. Kormendy & Kennicutt 2004) are considered as possible processes driving the formation of bulges. According to theoretical models, these processes give rise to different properties of the stellar populations in galaxy centres and to different trends of age, metallicity, and star formation time-scale as a function of the galactocentric distance.

For example, from the metallicity gradient, it is possible to extract information about the gas dissipation processes and the importance of secular processes and merging history. Stars form at all galactocentric distances during the dissipative collapse of a protogalactic cloud and they remain on their orbits with little migration towards the centre. On the contrary, the gas dissipates inwards and it is continuously enriched by the evolving stars. In consequence of this, the stars formed in the outskirts of a galaxy are expected to have a lower metal contents with respect to those in the central regions. Also galactic winds induced by the supernovae (Arimoto & Yoshii 1987; Creasey, Theuns & Bower 2013) have a relevant role in the evolution history of the galaxy. High-resolution simulations (Hirschmann et al. 2013) demonstrated that the stellar accretion in galaxies with galactic winds is steepening the galactic gradient of about 0.2 dex (Hirschmann et al. 2015). These winds, indeed, eliminate the gas suppressing the fuel needed for star formation. The outer regions develop the winds before the central ones, where the star formation and chemical enrichment continue for a longer time. Strong negative gradients are expected in dissipative collapse models as both star formation and galactic winds act in steepening any incipient gradient. In hierarchical formation models, the situation is somewhat contradictory. Some authors suggest that clustering and wet or dry merging erase the metallicity gradient (e.g. Bekki & Shioya 1999; Di Matteo et al. 2009), while others argue

⋆ E-mail: lorenzo.morelli@unipd.it

that the metallicity gradient is moderately affected by interactions since the violent relaxation preserves the position of the stars in the local potential (e.g. van Albada 1982). Such a dichotomy possibly depends on how the properties of the resulting galaxy are related to the gas-to-stellar mass ratio of the progenitors. If they are characterized by a large gas fraction, the resulting metallicity gradient is indeed steeper. In the secular evolution scenario, the bulge is the result of a redistribution of the disc stars due to the instabilities triggered by bars, ovals, and spiral arms. The theoretical model predictions for the metallicity gradient in these bulges are ambiguous. It could be erased as consequence of disc heating or amplified from the reduction of the scalelength of the final resulting spheroid (Moorthy & Holtzman 2006).

In the last decade, a major observational effort was performed to derive the stellar population properties in large number of bulges (e.g. Jablonka, Gorgas & Goudfrooij 2007; Morelli et al. 2008, 2012; González Delgado et al. 2014; Seidel et al. 2015; Wilkinson et al. 2015) to be compared to those of elliptical galaxies (e.g. Sánchez-Blázquez et al. 2006; Annibali et al. 2007; Kuntschner et al. 2010; McDermid et al. 2015) and galaxy discs (Sánchez-Blázquez et al. 2014; Morelli et al. 2015). Stellar populations of bulges show a complex variety of properties. The ages of bulges are spread between 1 and 15 Gyr. Such a large difference seems to be driven by the morphological type of the host galaxy with the late type younger than the early type (Ganda et al. 2007). The time-scale of the last major star formation burst spans between 1 and 5 Gyr, as derived from the central values of α/Fe abundance ratio (Thomas & Davies 2006). In general, α/Fe is constant over the observed radial ranges and many bulges have a solar abundance ratio (Jablonka et al. 2007; Morelli et al. 2008, 2012). Independently of their structural properties and whether they reside in low- or high-surface brightness discs, most bulges are characterized by a negative metallicity gradient, which is one of the tighter predictions made by theoretical models for the dissipative collapse (Gilmore & Wyse 1998; Pipino et al. 2010). On the other hand, the absence of stellar population gradients measured in some bulges is an clear indication that bulge stars were redistributed as a consequence of external and internal processes, like minor mergers and slow rearrangement of the disc material, respectively (Bekki & Shioya 1999; Kobayashi & Arimoto 1999).

In many cases, the difficulty in determining the mechanism driving the assembly history of the bulge is probably due to the fact that the dissipative collapse, minor and major mergers, and secular evolution are all having an effect in reshaping the structure of disc galaxies. Furthermore, phenomena driven by the environment like gas stripping, harassment, and strangulation are likely to play a role in mixing up the properties of the stellar populations (La Barbera et al. 2014). However, to date, the observational evidences on how the environment influences the stellar populations of bulges are sparse and the analysis of both the central values of age, metallicity, and star formation time-scale (Denicoló et al. 2005; Reda et al. 2007) and their radial gradients (Katkov, Kniazev & Sil'chenko 2015) does not lead to any firm conclusion. In addition, the comparison of the results obtained for galaxies in different environments is not straightforward. Part of the difficulty lies in addressing the relative importance of one-to-one interactions and the local galaxy density, and this reflects the lack of suitable control samples to which the properties of bulges of interacting and/or cluster galaxies can be compared. As a matter of fact, the samples of field galaxies studied so far include also the galaxies in pairs and loose groups.

A way to make the observational picture simpler is studying the bulges of isolated galaxies, for which the interactions with the surrounding environment or with other galaxies are likely to be negligible (Hirschmann et al. 2013). Therefore, it could be possible to use the stellar population diagnostics to disentangle between bulges formed from dissipative collapse and those assembled via secular evolution. To this aim, here we analyse the stellar populations of the bulges of a carefully selected sample of high-surface brightness isolated disc galaxies to be compared with the complementary samples of bulges in high-surface brightness cluster galaxies and giant low-surface brightness galaxies which we studied in in the past several years (Morelli et al. 2008, 2012, 2015; Pizzella et al. 2008).

The paper is organized as follows. We present the selection of the sample of isolated disc galaxies in Section 2, and we describe the analysis of the photometric and spectroscopic data in Sections 3 and 4, respectively. We analysed the stellar population properties in Section 5. We discuss conclusions and summarize results in Section 6.

2 SAMPLE SELECTION

We selected the sample galaxies from the Catalogue of Isolated Galaxies (CIG; Karachentseva 1973). The CIG comprises 1051 galaxies with apparent magnitude $M_{ZW} < 15.7$ and $\delta < -3°$. In the CIG are included galaxies with radius R and with no other galaxy with radius $1/4R < r < 4R$ within a projected distance of $40r$. Assuming an average radius of $R = 10$ kpc and an average field velocity of $V = 150$ km s^{-1}, the CIG galaxies should not have passed close to a mass perturber in the last 3×10^9 yr. We mined the CIG to find nearby ($D < 150$ Mpc) early-to-intermediate disc galaxies (from S0 to Sbc) in order to spatially resolve the bulge component. They were chosen to have a low-to-intermediate inclination ($i < 70°$) to allow a reliable photometric decomposition, available images in the Sloan Digital Sky Survey (SDSS; York et al. 2000), and to be spectroscopically observed at the Telescopio Nazionale Galileo (TNG, $\delta > 0°$) Our final sample consist of 16 spiral galaxies, with multiband photometry already available and which are fully representative of the whole CIG sample. We actually observed 12 galaxies at the TNG telescope and they constitute the sample of isolated galaxies we studied in this paper. We report their basic properties in Table 1.

In Fig. 1, we compare the properties the morphological type, bulge-to-disc ratio (B/D) and central velocity dispersion of the sample galaxies with those of the group and cluster galaxies analysed by Morelli et al. (2008).

3 BROAD-BAND IMAGING

3.1 Data reduction

We retrieved the *i*-band images of the sample galaxies from the Data Archive Server of the SDSS Data Release 9 (Ahn et al. 2012). The images were reduced using IRAF[1] routines and trimmed selecting a field of view (FOV) of at least 400×400 pixels (corresponding to 2.6×2.6 arcmin^2) centred on the galaxies.

To estimate the goodness of the SDSS sky subtraction, we measured the surface brightness radial profile of the galaxies at large

---

[1] Image reduction and Analysis Facility is distributed by the National Optical Astronomy Observatories, which are operated by the Association of Universities for Research in Astronomy under cooperative agreement with the National Science Foundation.

Table 1. Parameters of the sample galaxies. The columns show the following. (1): galaxy name; (2): morphological classification from Lyon Extragalactic Database (LEDA); (3): numerical morphological type from LEDA; (4): apparent isophotal diameter measured at a surface brightness level of $\mu_B = 25$ mag arcsec^{-2} from LEDA; (5): total observed blue magnitude from LEDA; (6): radial velocity with respect to the cosmic microwave background (CMB) reference frame from LEDA; (7): distance obtained as V_{CMB}/H_0 with $H_0 = 75$ km s^{-1} Mpc^{-1}; (8): absolute total blue magnitude from B_T corrected for extinction as in LEDA and adopting D.

| Galaxy	Type	T	$D_{25} \times d_{25}$ (arcmin)	B_T (mag)	V_{CMB} (km s^{-1})	D (Mpc)	M_{B_T} (mag)
(1)	(2)	(3)	(4)	(5)	(6)	(7)	(8)
CGCG 034-050	Sb	1.0	0.95×0.52	14.53	3808	50.7	−18.99
CGCG 088-060	S0a	0.0	0.83×0.67	15.21	4725	63.0	−18.79
CGCG 152-078	E/S0	−2.8	0.48×0.47	15.81	6227	83.0	−18.78
CGCG 206-038	S0a	−0.5	0.81×0.69	14.86	6103	81.3	−19.69
IC 2473	Sbc	3.5	1.07×0.74	14.72	8325	111.0	−20.50
NGC 2503	Sbc	4.0	0.95×0.79	14.80	5711	76.1	−19.61
NGC 2712	SBb	3.1	2.95×1.58	12.78	2001	26.7	−19.35
NGC 2955	SABb	3.2	1.50×0.82	13.58	7254	96.7	−21.34
UGC 4000	SABb	2.9	1.44×0.46	14.88	9491	126.5	−20.63
UGC 4341	S0a	−0.1	1.17×0.59	14.66	6081	81.1	−19.88
UGC 5026	S0	−2.0	0.91×0.62	14.30	4480	59.7	−19.57
UGC 5184	Sb	3.0	1.02×0.65	14.73	6806	90.7	−20.05
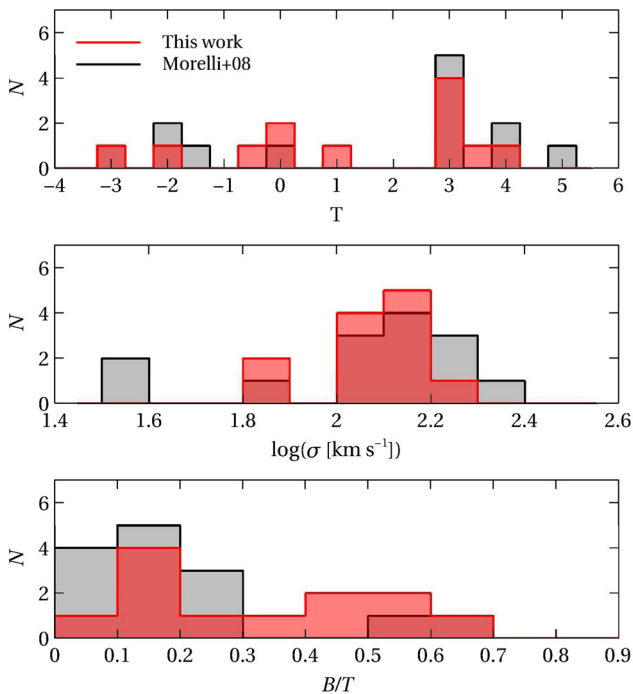
Figure 1. Distribution of the morphological type (upper panel), central velocity dispersion (middle panel), and B/D ratio (lower panel) for the sample galaxies (red histograms). The distribution of the same quantities for the group and cluster galaxies studied by Morelli et al. (2008) is plotted for a comparison (grey histograms).

radii by fitting their isophotes with ellipses using the ELLIPSE algorithm described by Jedrzejewski (1987). We masked foreground stars, nearby and background galaxies, residual cosmic rays, and bad pixels in each galaxy image before fitting the galaxy isophotes. As a first step, we allowed to vary the centres, ellipticities, and position angles of fitting ellipses. Then, we adopted the centre of the inner ellipses in the galaxy nucleus ($a < 5$ arcsec) and the ellipticity and position angle of the outer ones in the galaxy outskirts ($a > 10$ arcsec). We assumed the constant value of the surface brightness

measured at large radii ($a \sim 50$ arcsec where there was no light contribution from the galaxy) as the residual sky level to be subtracted from the image. We measured the standard deviation of the image background after sky subtraction, σ_{sky}, in regions free of sources at the edges of the FOV.

Finally, we ran ELLIPSE on the sky-subtracted images to derive the radial profiles of the azimuthally averaged surface brightness, μ, ellipticity, ϵ, and position angle, PA, of the galaxy isophotes. These profiles and the mask images were adopted for the photometric decomposition.

3.2 Photometric decomposition

The structural parameters of the bulge, disc, and bar components of the sample galaxies were derived from the sky-subtracted and masked images by applying the Galaxy Surface Photometry Two-Dimensional Decomposition (GASP2D) algorithm (Méndez-Abreu et al. 2008, 2014).

We modelled the surface brightness of the bulge, disc, and bar using a Sérsic (1968), Freeman (1970), and Ferrers (1877, see also Aguerri, Méndez-Abreu & Corsini 2009 for the choice of the shape parameter) function, respectively. More details of the procedures and algorithm used to retrieve the structural parameters of the sample galaxies can be found in Morelli et al. (2012).

In our analysis, we did not take into account for any other galaxy component, such as spiral arms or inner and outer rings. Despite that their inclusion in the galaxy model slightly modifies the best-fitting values of the structural parameters of our bulges, they result in a less constrained solution due to the increase of free parameters. In order to reduce the influence of these components on the fit, we masked their corresponding regions in the galaxy images and excluded them from the fitting process.

A bar was adopted for CGCG 088-060, CGCG 206-038, and IC 2473, whereas we do not include the bar to build the surface brightness models of the other sample galaxies. The best-fitting parameters were used to determine the radius r_{bd}, where half of the total surface brightness is due to the bulge only. Since we measured the bulge kinematics and stellar population from long-slit spectra, the r_{bd} value has to be determined along the slit direction which was

Table 2. Photometric parameters of the bulges of the sample galaxies. The columns show the following. (2): effective surface brightness; column (3): effective radius; column (4): shape parameter; column (5): axial ratio; column (6): position angle of the major axis; (7): bulge-to-total luminosity ratio; (8): radius where the bulge contributes half of the galaxy surface brightness.

Galaxy	μ_e (mag arcsec^{-2})	r_e (arcsec)	n	q_b	PA$_b$ ($°$)	B/T	r_{bd} (arcsec)
(1)	(2)	(3)	(4)	(5)	(6)	(7)	(8)
CGCG 034-050	18.38 ± 0.12	2.93 ± 0.10	2.57 ± 0.15	0.55 ± 0.09	37.54 ± 0.10	0.56	5.7
CGCG 088-060	18.70 ± 0.12	1.50 ± 0.10	1.85 ± 0.15	0.95 ± 0.09	1.46 ± 0.10	0.26	2.4
CGCG 152-078	19.09 ± 0.12	1.68 ± 0.10	3.48 ± 0.15	0.92 ± 0.09	102.64 ± 0.10	0.49	3.8
CGCG 206-038	18.44 ± 0.12	2.09 ± 0.10	1.27 ± 0.15	0.85 ± 0.09	54.94 ± 0.10	0.41	2.8
IC 2473	18.87 ± 0.12	1.98 ± 0.10	1.31 ± 0.15	0.81 ± 0.09	30.75 ± 0.10	0.18	3.7
NGC 2503	22.89 ± 0.12	8.84 ± 0.10	4.26 ± 0.15	0.54 ± 0.09	153.67 ± 0.10	0.11	1.8
NGC 2712	18.12 ± 0.06	2.22 ± 0.06	0.99 ± 0.10	0.66 ± 0.05	1.72 ± 0.05	0.09	3.8
NGC 2955	23.10 ± 0.12	26.60 ± 0.10	5.56 ± 0.10	0.72 ± 0.09	0.00 ± 0.10	0.59	4.1
UGC 4000	20.64 ± 0.12	4.12 ± 0.10	2.69 ± 0.10	0.83 ± 0.09	27.60 ± 0.10	0.33	4.2
UGC 4341	18.61 ± 0.12	2.06 ± 0.10	1.30 ± 0.10	0.73 ± 0.09	39.62 ± 0.10	0.18	2.3
UGC 5026	20.64 ± 0.12	9.49 ± 0.10	3.85 ± 0.10	0.48 ± 0.09	12.62 ± 0.10	0.69	6.1
UGC 5184	19.25 ± 0.12	1.53 ± 0.10	1.66 ± 0.10	0.71 ± 0.09	98.78 ± 0.10	0.10	1.2

Table 3. Photometric parameters of the discs of the sample galaxies. The columns show the following. (2): central surface brightness; (3): scalelength; (4): axial ratio; (5): position angle of the major axis; (6): disc-to-total luminosity ratio.

Galaxy	μ_0 (mag arcsec^{-2})	h (arcsec)	q_{disc}	PA$_{disc}$ ($°$)	D/T
(1)	(2)	(3)	(4)	(5)	(6)
CGCG 034-050	19.42 ± 0.11	7.48 ± 0.10	0.51 ± 0.10	35.39 ± 0.10	0.44
CGCG 088-060	20.32 ± 0.11	8.87 ± 0.10	0.76 ± 0.10	36.65 ± 0.10	0.65
CGCG 152-078	20.57 ± 0.11	6.32 ± 0.10	0.89 ± 0.10	122.65 ± 0.10	0.51
CGCG 206-038	20.88 ± 0.11	10.69 ± 0.10	0.29 ± 0.10	157.33 ± 0.10	0.18
IC 2473	20.52 ± 0.11	13.28 ± 0.10	0.66 ± 0.10	88.42 ± 0.10	0.69
NGC 2503	20.34 ± 0.11	11.98 ± 0.10	0.87 ± 0.10	2.20 ± 0.10	0.89
NGC 2712	19.35 ± 0.05	19.43 ± 0.06	0.55 ± 0.04	13.49 ± 0.06	0.91
NGC 2955	19.59 ± 0.11	12.47 ± 0.10	0.38 ± 0.10	154.95 ± 0.10	0.41
UGC 4000	20.21 ± 0.11	12.94 ± 0.10	0.34 ± 0.10	35.76 ± 0.10	0.67
UGC 4341	18.96 ± 0.11	9.95 ± 0.10	0.42 ± 0.10	47.81 ± 0.10	0.82
UGC 5026	19.22 ± 0.11	6.06 ± 0.10	0.50 ± 0.10	26.41 ± 0.10	0.30
UGC 5184	19.12 ± 0.11	8.63 ± 0.10	0.44 ± 0.10	107.24 ± 0.10	0.90

Table 4. Photometric parameters of the bars of the sample galaxies. The columns show the following. (2): central surface brightness; (3): length; (4): axial ratio; (5): position angle of the major axis; (6): bar-to-total luminosity ratio.

Galaxy	μ_{bar} (mag arcsec^{-2})	r_{bar} (arcsec)	q_{bar}	PA$_{bar}$ ($°$)	Bar/T
(1)	(2)	(3)	(4)	(5)	(6)
CGCG 088-060	20.52 ± 0.14	12.59 ± 0.15	0.39 ± 0.10	39.30 ± 0.10	0.08
CGCG 206-038	20.93 ± 0.14	26.36 ± 0.15	0.78 ± 0.10	143.76 ± 0.10	0.41
IC 2473	21.24 ± 0.14	37.04 ± 0.15	0.21 ± 0.10	83.47 ± 0.10	0.13

always chosen to be aligned with the galaxy major axis (Table 5). To this aim, we built a point spread function (PSF)-convolved image for each galaxy component using the structural parameters from the photometric decomposition. We computed r_{bd} by comparing the surface brightness profiles of the components we extracted along a 1-pixel wide strip crossing the galaxy centre and aligned with the galaxy major axis. We list the structural parameters of the bulges together with the radius r_{bd} in Table 2.

The structural parameters of the discs and bars are given in Tables 3 and 4, respectively.

We show the GASP2D fits and results of the photometric decomposition of the SDSS images of the sample galaxies in Fig. A1.

To derive the uncertainties on the structural parameters, we adopted a series of Monte Carlo simulations as done in Morelli et al. (2012, 2015). We generated a set of barred and unbarred galaxies with a total i-band magnitude within $11.5 \leq i_T \leq 14.5$ mag, mimicking the instrumental setup of the SDSS images. We randomly chose the structural parameters of the artificial galaxies to cover the ranges obtained for our galaxies with

$$0.1 \leq r_e \leq 13 \, \text{kpc}, \quad 0.4 \leq q_{bulge} \leq 1.0, \quad \text{and} \quad 0.5 \leq n \leq 6.5 \tag{1}$$

for the Sérsic bulges,

$$1 \leq h \leq 8 \, \text{kpc} \quad \text{and} \quad 0.2 \leq q_{disc} \leq 0.9 \tag{2}$$

Table 5. Log of the spectroscopic observations. The columns show the following. (2): date; (3): number and exposure time of the single exposures; (4): total exposure time; (5): slit position angle.

Galaxy	Date	Single exp. T. (s)	Total. exp. T. (h)	PA (°)
(1)	(2)	(3)	(4)	(5)
CGCG 034-050	2012/01/21	3×2400	2.0	37.1
CGCG 088-060	2012/01/23	4×2400	2.6	32.5
CGCG 152-078	2012/01/23	3×2400	2.0	120.0
CGCG 206-038	2012/01/22	3×2400	2.0	150.0
IC 2473	2012/01/21	3×2400	2.0	95.9
NGC 2503	2012/01/23	4×2400	2.6	4.5
NGC 2712	2012/01/20	3×2400	2.0	4.3
NGC 2955	2012/01/20	5×1800	2.5	159.4
UGC 4000	2012/01/20	3×2400	2.0	37.4
UGC 4341	2012/01/22	3×2400	2.0	45.3
UGC 5026	2012/01/22	3×2400	2.0	22.8
UGC 5184	2012/01/22	3×2400	2.0	84.8

for Freeman disc,

$$3 \leq r_{bar} \leq 21 \text{ kpc and } 0.2 \leq q_{bar} \leq 0.8 \tag{3}$$

for the Ferrers bars, and

$$q_{bar} \leq q_{disc} \leq q_{bulge}. \tag{4}$$

We assumed the artificial galaxies to be at a distance of 80 Mpc corresponding to a spatial scale of 388 pc arcsec^{-1}. We added to the simulated images a background level (120 ADU) and photon noise to yield a signal-to-noise ratio similar to that of the SDSS ones. Finally, the simulated images were convolved with a Moffat PSF with FWHM = 2.77 pixels and $\beta = 3.05$. We analysed the images of the artificial galaxies with GASP2D as if they were real and the systematic and typical errors for the best-fitting parameters were derived as in Morelli et al. (2015). The computed errors account for the systematic as well as the parameter covariance errors. However, they do not include possible deviations from the actual solution due to the presence of additional galaxy components, such as spiral arms or rings.

4 LONG-SLIT SPECTROSCOPY

4.1 Observations and data reduction

We carried out the spectroscopic observations of the sample galaxies with 3.6-m TNG telescope at the Observatorio del Roque de los Muchachos in La Palma (Spain) on 2012 January 20–23. The low-resolution spectrograph (DOLORES) mounted the volume phase holographic VHR-V grism with 566 grooves mm^{-1} in combination with the 0.7 arcsec $\times$ 8.1 arcmin slit and the thinned back-illuminated E2V CCD with 2048 $\times$ 2048 pixels of 13.5 $\times$ 13.5 μm^2. The spectral range covered from 4700 to 6750 Å. The reciprocal dispersion was 0.95 Å pixel^{-1} and the measured instrumental dispersion after the wavelength calibration was 2.7 Å (full width at half-maximum, FWHM). This corresponds to $\sigma_{inst} \sim 60$ km s^{-1} at 5725 Å. The angular sampling was 0.252 arcsec pixel^{-1}.

We observed the sample galaxies along the major axis. The value of the seeing FWHM measured on the guide star during the observation ranged between 0.7 and 1.5 arcsec. The integration time of each exposure, total integration time, and slit position angle of the galaxy spectra are given in Table 5. We also observed a number of giant stars selected from the sample by Worthey et al. (1994) to use

their spectra as templates for calibrating the line-strength indices. In addition, we obtained different spectra of a least one spectrophotometric standard star per night to calibrate the flux of the galaxy and template star.

The spectroscopic data reduction was performed using standard IRAF routines as done in Morelli et al. (2012). In this case, we corrected the rebinned spectra for the wavelength shift arising from DOLORES flexures, which produce shifts of the arc-lamp emission lines as a function of derotator angle (Marinoni et al. 2013). We finally measured an error of 0.3 Å in the wavelength calibration resulting in an accuracy of $\sim$2 km s^{-1} at 5725 Å.

4.2 Stellar kinematics

We measured the line-of-sight velocity distribution (LOSVD) of the stellar component of the sample galaxies from the absorption lines in the observed wavelength range using the Penalized Pixel Fitting (PPXF; Cappellari & Emsellem 2004) and Gas and Absorption Line Fitting (GANDALF; Sarzi et al. 2006) IDL codes which we adapted to deal with TNG spectra. The LOSVD was assumed to be a Gaussian plus third- and fourth-order Gauss–Hermite polynomials (Gerhard 1993; van der Marel & Franx 1993).

We rebinned each galaxy spectrum along the dispersion direction to a logarithmic scale, and along the spatial direction to obtain an S/N $\geq$ 20 per resolution element. For each radial bin, we built an optimal template spectrum by convolving a linear combination of simple stellar population (SSP) spectra (Vazdekis et al. 2010) based on the Medium Resolution Isaac Netwon Telescope Library of Empirical Spectra (MILES; Sánchez-Blázquez et al. 2006) with the LOSVD in order to fit the galaxy spectrum. The optimal template spectrum and LOSVD moments were obtained by χ^2 minimization in pixel space. Before fitting, the SSP spectra were logarithmically rebinned and de-reshifted to rest frame. Moreover, we degraded the spectral resolution of the galaxy spectrum by convolving it with a Gaussian function in order to match the MILES spectral resolution (FWHM = 2.5 Å; Beifiori et al. 2011; Falcón-Barroso et al. 2011) . In addition, we simultaneously fitted the ionized-gas emission lines detected with an S/N > 3. We masked the bad pixels coming from imperfect subtraction of sky emission lines and excluded them from the fitting procedure. We added a low-order multiplicative Legendre polynomial to correct for the different shape of the continuum in the spectra of the galaxy and optimal template due to reddening and large-scale residuals of flat-fielding and sky subtraction.

By measuring the LOSVD moments in all the available radial bins along the spatial direction, we derived the radial profiles of the LOS velocity v, velocity dispersion σ, third- and fourth-order Gauss–Hermite moments h_3 and h_4 of the stars. We estimated the uncertainties on the LOSVD moments running Monte Carlo simulations. For each radial bin, we built a set of simulated galaxy spectra by randomly perturbing the best-fitting galaxy spectrum. We added to the counts of each pixel of the best-fitting galaxy spectrum a random value chosen from a Gaussian distribution with a mean of zero and the same standard deviation of the difference between the observed and best-fitting galaxy spectra in the wavelength range used in the fit and excluding the emission lines. We measured the simulated spectra as if they were real. For each LOSVD moment, we adopted as error the standard deviation of the distribution of the values derived for the simulated galaxy spectra. We found no bias of the PPXF method with the adopted instrumental setup and spectral sampling in the ranges of S/N and σ which characterize the spectra of the sample galaxies. Indeed, the values of h_3 and h_4 measured in a set of simulated galaxy spectra obtained by convolving the

Table 6. Central values of the velocity dispersion and line-strength indices of the sample galaxies measured within an aperture of radius $0.3\,r_e$.

Galaxy (1)	σ (km s^{-1}) (2)	$\langle$Fe$\rangle$ (Å) (3)	[MgFe]$'$ (Å) (4)	Mg$_2$ (mag) (5)	Mg$_b$ (Å) (6)	Hβ (Å) (7)
CGCG 034-050	112.6 ± 28.8	2.801 ± 0.137	3.630 ± 0.036	0.299 ± 0.004	4.642 ± 0.144	1.334 ± 0.117
CGCG 088-060	65.4 ± 7.5	2.896 ± 0.131	3.400 ± 0.032	0.241 ± 0.004	3.932 ± 0.144	1.969 ± 0.114
CGCG 152-078	108.6 ± 4.4	2.860 ± 0.132	3.465 ± 0.023	0.246 ± 0.005	4.081 ± 0.102	1.838 ± 0.092
CGCG 206-038	147.2 ± 6.1	3.271 ± 0.142	3.960 ± 0.041	0.290 ± 0.004	4.775 ± 0.147	1.331 ± 0.116
IC 2473	136.2 ± 11.9	1.710 ± 0.304	2.036 ± 0.076	0.130 ± 0.006	2.505 ± 0.244	1.792 ± 0.220
NGC 2503	77.6 ± 9.7	2.350 ± 0.299	2.623 ± 0.097	0.166 ± 0.007	2.857 ± 0.247	2.413 ± 0.236
NGC 2712	108.2 ± 8.6	2.244 ± 0.155	2.653 ± 0.034	0.161 ± 0.004	3.052 ± 0.166	2.294 ± 0.116
NGC 2955	128.2 ± 10.7	1.900 ± 0.265	2.236 ± 0.061	0.139 ± 0.007	2.616 ± 0.207	3.153 ± 0.168
UGC 4000	147.4 ± 10.6	2.203 ± 0.337	2.982 ± 0.182	0.217 ± 0.009	3.981 ± 0.362	1.009 ± 0.265
UGC 4341	192.5 ± 6.2	2.771 ± 0.167	3.610 ± 0.060	0.268 ± 0.005	4.595 ± 0.200	1.469 ± 0.173
UGC 5026	121.9 ± 3.1	2.575 ± 0.145	2.975 ± 0.029	0.194 ± 0.004	3.371 ± 0.134	2.428 ± 0.116
UGC 5184	130.9 ± 8.4	1.875 ± 0.237	2.405 ± 0.066	0.128 ± 0.007	2.803 ± 0.232	2.022 ± 0.201

best-fitting galaxy spectrum with a Gauss–Hermite LOSVD, and adding photon, readout, and sky noise to mimic actual observations differ from the intrinsic ones only within the estimated errors. We give the measured stellar kinematics in Table A1 and plot the folded profiles of v, σ, h_3, and h_4 as a function of radius in Fig. A2.

The regularity and symmetry of the kinematic profiles is a further indication that the sample galaxies are isolated and have not recently experienced merging or interaction with other galaxies (e.g. Barton, Bromley & Geller 1999).

4.3 Line-strength indices

We measured the Mg, Fe, and Hβ line-strength indices of the Lick/IDS system (Faber et al. 1985; Worthey et al. 1994), the iron index $\langle$Fe$\rangle = (\mathrm{Fe}5270 + \mathrm{Fe}5335)/2$ (Gorgas, Efstathiou & Salamanca 1990), the combined magnesium–iron index [MgFe]$' = \sqrt{\mathrm{Mg}b\,(0.72 \times \mathrm{Fe}5270 + 0.28 \times \mathrm{Fe}5335)}$ (Thomas, Maraston & Bender 2003) and their errors by following the same procedure and method adopted by Morelli et al. (2004, 2015). The offsets between our line-strength measurements and Lick/IDS line-strength values (Worthey et al. 1994) were smaller than the mean error of the differences and therefore we did not apply any offset correction to our line-strength measurements. We list in Table A1 and plot in Fig. A3 the measured values of Hβ, [MgFe]$'$, $\langle$Fe$\rangle$, Mg$_b$, and Mg$_2$ as a function of radius for all the sample galaxies.

We derived the central values of Mg$_b$, Mg$_2$, Hβ, $\langle$Fe$\rangle$, and [MgFe]$'$ as an S/N-weighted mean of the values measured within an aperture of radius $0.3\,r_e$ along the major axis of the galaxies. Similarly, we derived the central value of the velocity dispersion. The central values of σ, Mg$_b$, Mg$_2$, Hβ, $\langle$Fe$\rangle$, and [MgFe]$'$ are reported in Table 6.

Fig. 2 shows the correlations between the central values of the Hβ, $\langle$Fe$\rangle$, and Mg$_2$ line-strength indices with the central velocity dispersion for the sample galaxies. They are compared with the results obtained by Morelli et al. (2008) for the bulges of group and cluster galaxies.

Tight Mg$_2$–σ and $\langle$Fe$\rangle$–σ correlation have been predicted from theoretical models (e.g. Kodama et al. 1998) and observed in spheroids of galaxies being them early-type galaxies (see Fisher, Franx & Illingworth 1996; Jørgensen 1999; Trager et al. 1998; Mehlert et al. 2003) or bulges of spiral galaxies (Idiart, de Freitas Pacheco & Costa 1996; Prugniel, Maubon & Simien 2001; Proctor & Sansom 2002; Ganda et al. 2007; Morelli et al. 2012). The correlations, in general, show that more massive systems host a
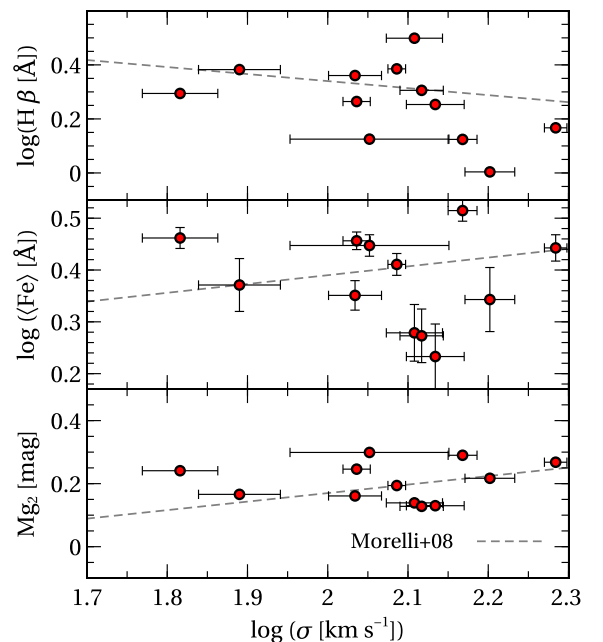

Figure 2. Central values of the Hβ (upper panel), $\langle$Fe$\rangle$ (middle panel), and Mg$_2$ (lower panel) line-strength indices measured over an aperture of $0.3\,r_e$ for the sample galaxies as a function of their central velocity dispersion. In each panel, the blue dashed line represents the correlation found by Morelli et al. (2008) for the bulges of galaxies in groups and clusters.

more metal-rich stellar population (Thomas et al. 2010). The values of the indices we obtained (Fig. 2) are consistent with the relations found for a similar sample of cluster galaxies by Morelli et al. (2008). We also found an anticorrelation between Hβ and σ in our sample of isolated galaxies as we did in Morelli et al. (2008, 2012). Less massive galaxies are, on average, younger than more massive galaxies and, in spite of the large scatter, this result is consistent with our previous works and with the findings of Ganda et al. (2007).

In Fig. 3, the distribution of the central values of Hβ, $\langle$Fe$\rangle$, and Mg$_b$ line-strength indices for the bulges of our sample of isolated galaxies is compared with the values obtained for the bulges of group and cluster galaxies of Morelli et al. (2008). The distributions are similar, although the Mg$_b$ values in the isolated galaxies seems to be slightly shifted to the higher end.
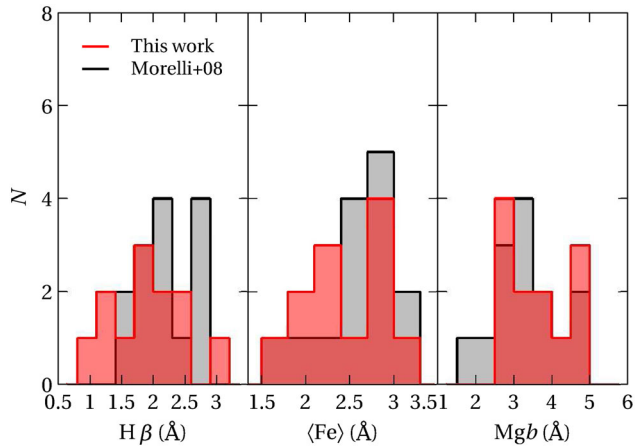
Figure 3. Distribution of the central values of the H β (left-hand panel), $\langle$Fe$\rangle$ (middle panel), and Mg$_b$ (right-hand panel) for the sample bulges (red histograms). The distribution of the same quantities for the bulges of group and cluster galaxies studied by Morelli et al. (2008) is plotted for a comparison (grey histograms).

5 PROPERTIES OF THE STELLAR POPULATIONS

5.1 Central values of age, metallicity, and α/Fe enhancement

We derived the stellar population properties in the centre of the sample galaxies by comparing the measurements of the line-strength indices with the model predictions by Thomas et al. (2003) for the single stellar population as a function of age, metallicity, and α/Fe enhancement. We plot the central values of Hβ, [MgFe]$'$, $\langle$Fe$\rangle$, and Mg$_b$ and model predictions in Fig. 4. We calculated the age, metallicity, and α/Fe enhancement in the centre of the sample galaxies from the central values of line-strength indices given in Table 6 by following Morelli et al. (2012).

We list the central values of age, metallicity, and α/Fe enhancement and their corresponding errors in Table 7 and show the histograms of their number distribution in Fig. 5.

We found that the ages of the sample bulges have a bimodal distribution (Fig. 5, left-hand panel) with about half of them being old (14–15 Gyr) and the remaining ones characterized by a young-to-intermediate age (1–5 Gyr). Such a large range of ages for the bulges of isolated galaxies is consistent with the results obtained by Katkov et al. (2015). We measured prominent emission lines, which are indicative of ongoing star formation, only in the centre of sample galaxies with younger bulges. The metallicity of the sample bulges spans a large range of values (Fig. 5, middle panel) from high ([Z/H] = 0.3 dex) to sub-solar metallicity ([Z/H] = -0.7 dex). On the contrary, the α/Fe enhancement of the sample bulges is characterized by a narrow distribution of supersolar values ([α/Fe] = 0.1–0.3 dex) peaked at [α/Fe] = 0.2 dex (Fig. 5, right-hand panel).

In Fig. 5, we compare the number distributions of the age, metallicity, and α/Fe enhancement of the bulges of our sample of isolated galaxies to those found by Morelli et al. (2008), who carried out a similar analysis on the bulge stellar populations of galaxies in groups and clusters. The isolated galaxies show a large fraction of very old bulges, which are not observed in group and cluster galaxies. There is no difference in the bulge metallicity distribution for most of the isolated galaxies with respect to the group and cluster galaxies, except for a couple of bulges with a very low metallicity. The most significant difference between the bulges of isolated
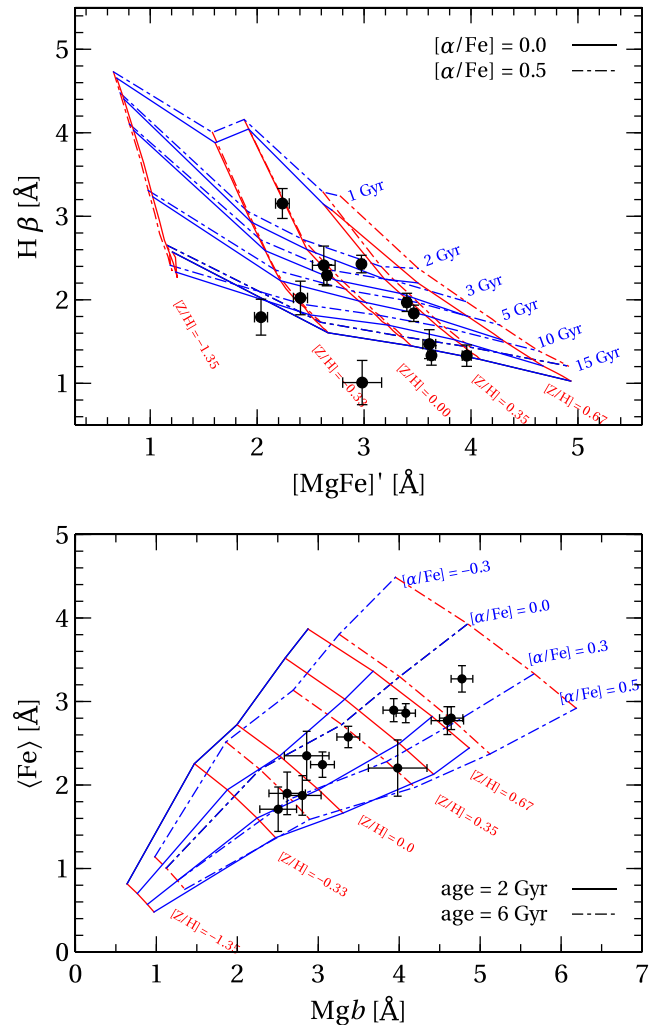
Figure 4. Distribution of the central values of Hβ and [MgFe]$'$ indices (top panel) and $\langle$Fe$\rangle$ and Mg$_b$ indices (bottom panel) for the sample galaxies. The lines indicate the models by Thomas et al. (2003).

Table 7. Mean age, total metallicity, and total α/Fe enhancement of the stellar populations of the bulges of the sample galaxies.

| Galaxy	Age	[Z/H]	[α/Fe]
	(Gyr)	(dex)	(dex)
(1)	(2)	(3)	(4)
CGCG 034-050	15.0 ± 3.2	0.05 ± 0.07	0.22 ± 0.05
CGCG 088-060	4.0 ± 1.4	0.30 ± 0.09	0.12 ± 0.06
CGCG 152-078	5.4 ± 1.7	0.27 ± 0.07	0.15 ± 0.06
CGCG 206-038	14.9 ± 3.8	0.28 ± 0.09	0.11 ± 0.05
IC 2473	>15.0	-0.65 ± 0.10	0.21 ± 0.15
NGC 2503	2.6 ± 1.3	0.00 ± 0.12	0.08 ± 0.14
NGC 2712	3.2 ± 0.8	-0.05 ± 0.06	0.16 ± 0.07
NGC 2955	1.7 ± 0.2	-0.04 ± 0.07	0.24 ± 0.13
UGC 4000	>15.0	-0.19 ± 0.12	0.33 ± 0.11
UGC 4341	13.8 ± 4.8	0.12 ± 0.11	0.22 ± 0.06
UGC 5026	1.9 ± 0.4	0.26 ± 0.06	0.16 ± 0.05
UGC 5184	7.7 ± 2.5	-0.29 ± 0.07	0.26 ± 0.11
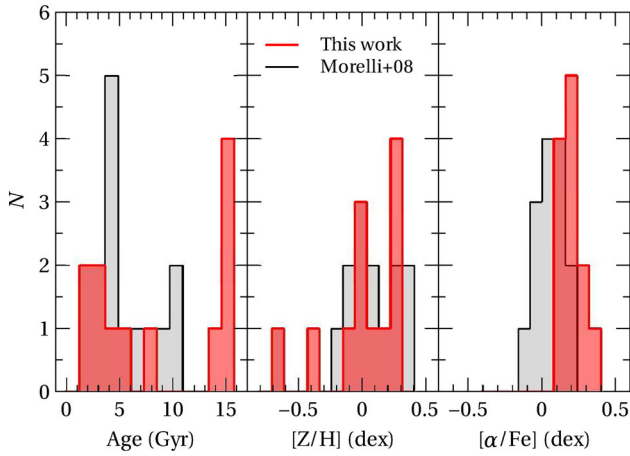
Figure 5. Distribution of the mean age (left-hand panel), total metallicity (central panel), and total α/Fe enhancement (right-hand panel) for the stellar population of the bulges of the sample galaxies (red histograms). The distribution of the same quantities for the bulges of group and cluster galaxies studied by Morelli et al. (2008) is plotted for a comparison (grey histograms).

galaxies and those of group and cluster galaxies is represented by the very different distributions of their [α/Fe] ratios. The bulges of isolated galaxies have systematically higher values of α/Fe enhancement. This implies a difference in the star formation time-scale with the inner regions of isolated bulges being formed more rapidly with respect to bulges in high-density environments.

The metallicity and α/Fe enhancement are well correlated with the central velocity dispersion in early-type galaxies (Mehlert et al. 2003; Spolaor et al. 2010) and in bulges of high (Ganda et al. 2007; Morelli et al. 2008) and low-surface brightness galaxies (Morelli et al. 2012). Cosmological hydrodynamic simulations (De Lucia, Kauffmann & White 2004; Tassis, Kravtsov & Gnedin 2008) and chemodynamical models (Matteucci 1994; Kawata & Gibson 2003; Kobayashi 2004) demonstrated that these relations are the result of a mass-dependent star formation efficiency. High-mass galaxies have a higher efficiency in converting gas-phase metals into new stars, giving rise to less prolonged star formation events and higher α/Fe enhancements. Our findings suggest that these results can be extended also to our isolated galaxies (Fig. 6). Our conclusion is that the most massive bulges of our sample are more metal-rich and characterized by a shorter star formation time-scale.

Finally, we looked for a possible correlation between the stellar population properties of the sample bulges and the morphological type of their host galaxies. Indeed, very shallow correlations were found by Ganda et al. (2007) and Morelli et al. (2008) whereas Thomas & Davies (2006) and Morelli et al. (2012) did not observe any trend. We did not find any correlation between the galaxy morphological type and age, metallicity, or α/Fe enhancement of bulges in isolated galaxies (Fig. 7). The absence of these correlations could be an indication that the stellar populations of the bulges and discs in isolated galaxies had an independent evolution.

3 out of 12 galaxies in our sample turned out to have a bar (Fig. A1). We found no correlation between the stellar population properties of the sample bulges and the presence of the bar. This could be a consequence that the bulge contribution is always dominating the light distribution inside r_{bd}. Similar results were found in Seidel et al. (2016) and are consistent with the theoretical
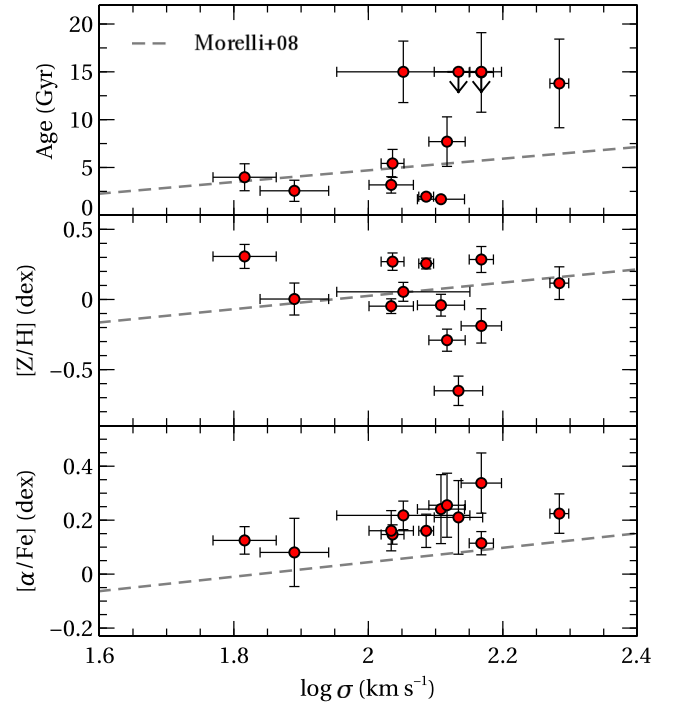

Figure 6. Mean age (upper panel), total metallicity (middle panel), and total α/Fe enhancement (lower panel) of the stellar populations of the bulges of the sample galaxies as a function of the central velocity dispersion. In each panel, the dashed line represents the correlation found by Morelli et al. (2008) for the bulges of group and cluster galaxies.
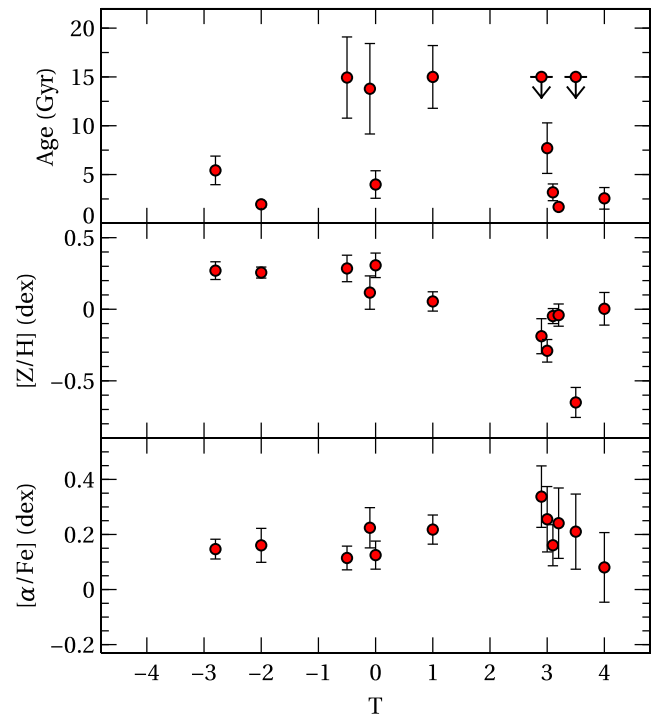

Figure 7. Mean age (upper panel), total metallicity (middle panel), and total α/Fe enhancement (lower panel) of the stellar populations of the bulges of the sample galaxies as a function of the galaxy morphological type.

predictions by Wozniak (2007) and observational findings by Pérez & Sánchez-Blázquez (2011) and James & Percival (2016).

5.2 Radial gradients of age, metallicity, and α/Fe enhancement

Theoretical models predict different radial gradients of age, metallicity, and α/Fe enhancement as consequence of different galaxy formation mechanisms. Therefore, the radial trends of the stellar population properties within bulges are one of the most important diagnostics to understand the processes regulating their assembly.

From the theoretical point of view, a steep metallicity gradient is expected in bulges forming through pure monolithic collapse scenarios (Eggen, Lynden-Bell & Sandage 1962; Larson 1974; Arimoto & Yoshii 1987) and their modern versions (Kawata 2001; Kobayashi 2004). Gas dissipation with subsequent occurrence of star formation and blowing of galactic winds produce the metallicity gradient. A relation between the steepening of the gradient and mass is also expected (Pipino et al. 2010). A strong gradient in the α/Fe enhancement is expected too (Ferreras & Silk 2002). However, Pipino, D'Ercole & Matteucci (2008) suggested that together with the outside-in scenario, other important processes need to be considered to explain the origin of the abundance ratios. In addition, they pointed out that the interplay between the star formation time-scale and the gas flows is very important, since it acts both in flattening the α/Fe gradient and in enabling the galaxy to harbour a metallicity gradient.

On the contrary, the metallicity gradient is expected to be very shallow or absent when it is investigated in merger-based models (Bekki & Shioya 1999). This is due to the fact that mergers mix up all the stars in the galaxy removing the gradients. Secondary star formation, eventually happening during a wet merger, only rarely steepens the gradient (Kobayashi 2004). If this happens, the age radial profile should maintain a clear signature for several Gyr (Hopkins et al. 2009), whereas dry mergers flatten all the preexisting gradients (Pipino et al. 2010).

Secular evolution predicts a variety of opposite results for the resulting gradients of the stellar populations as a consequence of the relative importance of different mechanisms acting in this scenario as discussed in Moorthy & Holtzman (2006).

An issue in measuring the gradients of the age, metallicity, and α/Fe enhancement in bulges could be the contamination of their stellar population by the light coming from the underlying disc stellar component. To account for the light contamination from the disc component, we mapped the radial gradients up to the radius r_{bd} where the surface brightness contribution of the bulge component is equal to the contribution from the other components. Although it was not possible to completely remove the contribution from the disc, limiting the analysis to the radius r_{bd} ensured us that the degree of contamination is the same across all the sample of galaxies.

Bulges can have a very complicate and peculiar structure (Peletier et al. 2007; Morelli et al. 2010; Corsini et al. 2012). We have carefully inspected the two-dimensional photometric decomposition and stellar kinematics of the sample galaxies to look for the presence of distinct structures in our bulges but we did not find any evidence of them. Furthermore, to avoid possible misleading results due to the presence of spiral arms or small star-forming regions, we adopted the following process to derive the gradients of the line-strength indices along the major axis of the sample galaxies. Following Mehlert et al. (2003), we derived the gradient of each line-strength index by fitting the data inside r_{bd}. The gradient was derived as the difference between the best-fitting value at r_{bd} and in the central

Table 8. Gradients of the Hβ, $\langle$Fe$\rangle$, and Mg$_b$ line-strength indices of the sample bulges derived from the values in the centre and at r_{bd}, where the surface brightness contributions of the bulge and remaining components are equal.

| Galaxy	r_{bd} (kpc)	Δ Hβ (Å r$_{bd}^{-1}$)	Δ $\langle$Fe$\rangle$ (Å r$_{bd}^{-1}$)	Δ Mg$_b$ (mag r$_{bd}^{-1}$)
(1)	(2)	(3)	(4)	(5)
CGCG 034-050	1.40	0.19 ± 0.16	-0.17 ± 0.19	-0.47 ± 0.21
CGCG 088-060	0.73	-0.24 ± 0.19	-0.34 ± 0.25	-0.82 ± 0.24
CGCG 152-078	1.52	0.02 ± 0.14	-0.10 ± 0.23	-0.37 ± 0.18
CGCG 206-038	1.10	0.03 ± 0.17	-0.23 ± 0.21	-0.64 ± 0.21
IC 2473	1.99	0.24 ± 0.31	0.53 ± 0.46	0.21 ± 0.37
NGC 2503	0.70	0.04 ± 0.33	0.25 ± 0.43	-0.22 ± 0.35
NGC 2712	0.50	-0.35 ± 0.19	0.03 ± 0.26	-0.37 ± 0.26
NGC 2955	1.92	-0.00 ± 0.24	-0.01 ± 0.37	0.02 ± 0.28
UGC 4000	2.57	-0.06 ± 0.40	0.14 ± 0.56	-0.07 ± 0.53
UGC 4341	0.90	-0.24 ± 0.25	-0.16 ± 0.26	-0.31 ± 0.30
UGC 5026	1.76	0.05 ± 0.17	-0.10 ± 0.24	-0.21 ± 0.21
UGC 5184	0.53	0.91 ± 0.35	0.17 ± 0.32	-0.34 ± 0.31
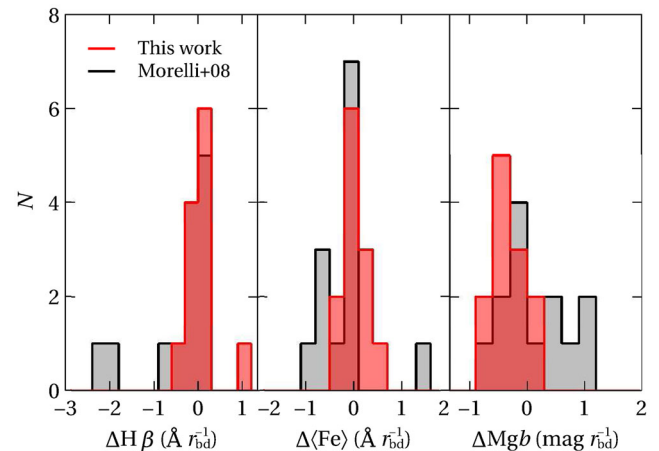
Figure 8. Distribution of the gradients of Hβ (left-hand panel), $\langle$Fe$\rangle$ (central panel), and Mg$_b$ (right-hand panel) for the sample bulges (red histograms). The distribution of the same quantities for the bulges of group and cluster galaxies studied by Morelli et al. (2008) is plotted for a comparison (grey histograms).

region within $0.1r_e$ (Morelli et al. 2008, 2012, 2015). The resulting values of gradients for the Hβ, $\langle$Fe$\rangle$, and Mg$_b$ line-strength indices are reported in Table 8 and their distributions are shown in Fig. 8. With few exceptions, the sample galaxies display flat radial profiles of Hβ and $\langle$Fe$\rangle$ and a negative gradient of Mg$_b$ (Table 8).

We then converted the derived values of line-strength indices to the corresponding age, metallicity, and α/Fe enhancement of the stellar population using the models by Thomas et al. (2003), as previously done for the central values. The gradient of each stellar population property was derived as the difference between the value derived at r_{bd} and the central value obtained within $0.1r_e$. The uncertainties on the resulting gradients were derived as done in Morelli et al. (2012). We report the gradients of age, metallicity, and α/Fe enhancement of the sample bulges are listed in Table 9 and plot their number distributions in Fig. 9.

Almost all the sample bulges show a null or very shallow age gradient with a distribution peaked at Δ(age) = 0. The only exception is the bulge of CGCG 034-050 (Δ(age) $= -5.1 \pm 4.7$ Gyr) because the bulges of both CGCG 088-060 and NGC 4341 are

Table 9. Gradients of mean age, total metallicity, and total α/Fe enhancement of the stellar populations of the sample bulges derived from the central values and values at the radius r_{bd} where the surface brightness contributions of the bulge and remaining components are equal.

| Galaxy	Δ(Age) (Gyr r_{bd}^{-1})	Δ([Z/H]) (dex r_{bd}^{-1})	Δ([α/Fe]) (dex r_{bd}^{-1})
(1)	(2)	(3)	(4)
CGCG 034-050	-5.11 ± 4.7	-0.10 ± 0.07	-0.04 ± 0.10
CGCG 088-060	4.60 ± 5.7	-0.37 ± 0.11	-0.12 ± 0.11
CGCG 152-078	0.99 ± 2.1	-0.21 ± 0.10	-0.10 ± 0.09
CGCG 206-038	2.25 ± 4.2	-0.29 ± 0.08	-0.08 ± 0.07
IC 2473	–	–	–
NGC 2503	-0.12 ± 4.2	0.02 ± 0.18	-0.10 ± 0.17
NGC 2712	1.00 ± 2.3	-0.11 ± 0.08	-0.09 ± 0.14
NGC 2955	0.01 ± 0.5	-0.00 ± 0.09	0.02 ± 0.17
UGC 4000	–	–	
UGC 4341	4.03 ± 4.2	-0.34 ± 0.19	-0.06 ± 0.12
UGC 5026	0.14 ± 0.9	-0.14 ± 0.07	-0.04 ± 0.10
UGC 5184	-1.81 ± 2.1	0.17 ± 0.13	-0.07 ± 0.19
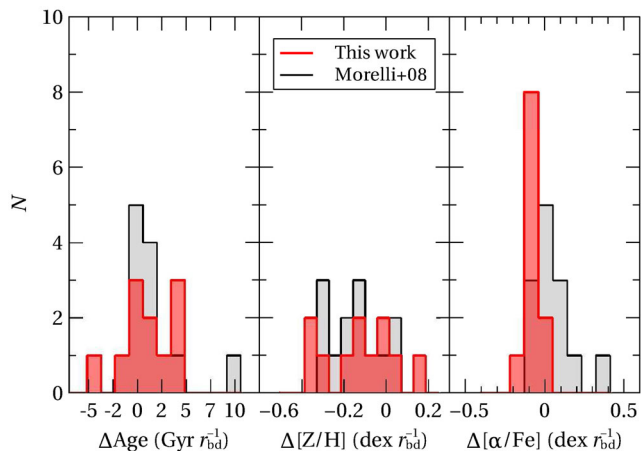
Figure 9. Distribution of the gradients of mean age (left-hand panel), total metallicity (central panel), and total α/Fe enhancement (right-hand panel) for the sample bulges (red histograms). The distribution of the same quantities for the bulges of group and cluster galaxies studied by Morelli et al. (2008) is plotted for a comparison (grey histograms).

consistent within the errors with Δ(age) = 0 in spite of their large age gradients. Our findings are in agreement with previous results for early-type galaxies (Mehlert et al. 2003; Sánchez-Blázquez et al. 2006; Spolaor et al. 2010) and late-type bulges (Jablonka et al. 2007). The number distribution of the age gradients of the bulges in isolated galaxies is remarkably similar to that of bulges in group and cluster galaxies (Fig. 9, left-hand panel) suggesting that the age distribution inside bulges is almost insensitive to environment.

The metallicity gradients of all the sample bulges are negative or null, with the exception of UGC 5184 that has a slightly positive gradient (Δ([Z/H]) = 0.17 dex). Negative metallicity gradients were also measured in early-type galaxies (Proctor & Sansom 2002; Mehlert et al. 2003; Sánchez-Blázquez, Gorgas & Cardiel 2006; Rawle, Smith & Lucey 2010) and in bulges of spiral galaxies (Jablonka et al. 2007; Morelli et al. 2015). They are expected for bulges assembled through a process of dissipative collapse (Kobayashi 2004). As for the age gradients, the number distributions of the metallicity gradients of the bulges hosted in isolated or in group and cluster galaxies are very similar to each other (Fig. 9,

central panel) suggesting the same formation scenario for bulges in different environments.

The gradients of α/Fe enhancement are negative or null for all the sample bulges and display a number distribution with a remarkable peak at Δ([α/Fe]) = -0.1 dex (Fig. 9, right-hand panel). This is a particularly interesting finding since it is in contrast with previous results obtained for early-type galaxies (Mehlert et al. 2003; Sánchez-Blázquez et al. 2006; Spolaor et al. 2010) bulges of unbarred (Jablonka et al. 2007) and barred galaxies (Sánchez-Blázquez et al. 2011; de Lorenzo-Cáceres et al. 2012), and bulges of group and cluster galaxies (Morelli et al. 2008). The [α/Fe] ratio is commonly used as a proxy of the star formation time-scale in galaxies (Thomas et al. 2005) because it is regulated by the different contributions to the enrichment of the interstellar medium caused by Type II and Type I supernovae (Matteucci & Greggio 1986). Therefore, we conclude that the star formation process was more prolonged in the outer parts of the sample bulges than in their central regions. Numerical simulations predict for dissipative collapse a strong inside-out formation process for bulges which gives rise to a negative gradient in the α/Fe enhancement (Ferreras & Silk 2002). Therefore, the negative gradients of α/Fe enhancement found in the bulges of isolated galaxies is consistent with the predictions of a dissipative collapse formation scenario.

We plot the central values and gradients of metallicity and α/Fe enhancement of the sample bulges in Fig. 10. As in Morelli et al. (2008) and Rawle et al. (2010), we found a tight linear correlation between the central values and gradients of metallicity (Fig. 10, left-hand panel) with a slope consistent with that given by Morelli et al. (2008). If confirmed with a larger sample of galaxies, this correlation is a further indication of the importance of dissipative collapse in the assembly of bulges (Arimoto & Yoshii 1987; Pipino et al. 2010). We did not find any correlation between the central values and gradients of α/Fe enhancement (Fig. 10, right-hand panel) as also pointed out by Morelli et al. (2008) and Rawle et al. (2010).

6 CONCLUSIONS

We analysed the surface brightness distribution, stellar kinematics, and stellar population properties of a sample of isolated galaxies selected from the CIG to constrain the dominant mechanism of the assembly of their bulges. To this aim, the properties of stellar populations of the sample bulges were compared with those of bulges in galaxies residing in groups and clusters.

A photometric decomposition of the SDSS i-band images was performed to obtain the structural parameters of the sample galaxies. We used the structural parameters to identify the bulge-dominated radial range of the sample galaxies by measuring the radius r_{bd}, where the bulge contribution to the galaxy surface brightness dominates over that of the remaining components.

We measured the stellar kinematics and radial profiles of the Mg_b, Mg_2, $H\beta$, and $\langle Fe \rangle$ line-strength indices from the major-axis spectra we obtained at TNG. The kinematics of all the sample galaxies is very regular giving further support to the idea that these objects are not suffering interactions with the neighbour galaxies. The correlations between the central values of the Mg_2 and $\langle Fe \rangle$ line-strength indices and velocity dispersion were found to be consistent with those for bulges of group and cluster galaxies (Idiart et al. 1996; Prugniel et al. 2001; Proctor & Sansom 2002; Morelli et al. 2008).

We obtained the stellar population properties of the bulges of the sample galaxies by deriving their central values of mean age, total metallicity, and total α/Fe from stellar population models
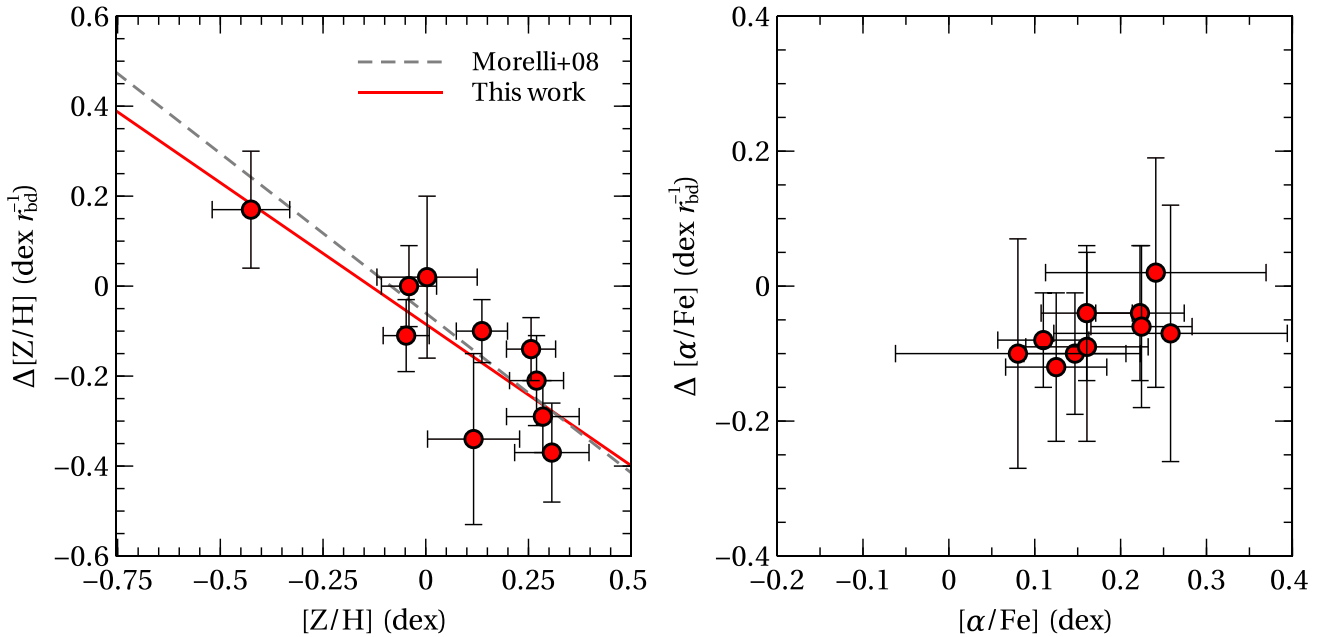
Figure 10. Gradient and central value of metallicity (left-hand panel) and α/Fe enhancement (right-hand panel) for the sample bulges. In the left-hand panel, the linear regression obtained for the bulges of the sample galaxies (red solid line) is compared to the correlation found by Morelli et al. (2008) for the bulges of galaxies in groups and clusters.

with variable element abundance ratios. The sample bulges are characterized by a bimodal age distribution with intermediate-age ($\sim$3 Gyr) and old systems ($\sim$15 Gyr), a large spread in metallicities ranging from sub- to supersolar values, and α/Fe enhancements peaked at $[\alpha/\text{Fe}] = 0.2$ dex. The higher $[\alpha/\text{Fe}]$ ratios found for the bulges of isolated galaxies indicate a shorter star formation time-scale with respect their counterparts in high-density environment (Thomas et al. 2005). On the contrary, the metallicity distribution is very similar for bulges residing in different environments.

The absence of a correlation between the bulge stellar populations and galaxy morphology excludes a strong interplay between bulges and discs during their evolution. This conclusion is also supported by the findings of Sil'chenko et al. (2012) and Katkov et al. (2015) who formulate the hypothesis that the morphological type of a field galaxy is determined by the outer-gas accretion. Finally, we derived the gradients of the stellar population properties within the sample bulges. Most of them have a null age gradient and a negative metallicity gradient. This is in agreement with earlier findings for bulges in cluster (Jablonka et al. 2007; Morelli et al. 2008) and high-surface brightness galaxies (Morelli et al. 2012). All the sample bulges show a negative gradient for the α/Fe enhancement. This is a prediction of the dissipative collapse model of bulge formation and it was never been observed before. The stellar population gradients are believed to be flattened or even erased by merging and acquisition events. Therefore, we suggest that the gradients imprinted during the inside-out formation process are preserved in the bulges of isolated galaxies, which suffered a limited number of interactions and mergers, whereas the gradients are cancelled in the bulges of group and cluster galaxies as a consequence of phenomena driven by environment.

ACKNOWLEDGEMENTS

REFERENCES

Aguerri J. A. L., Méndez-Abreu J., Corsini E. M., 2009, A&A, 495, 491
Ahn C. P. et al., 2012, ApJS, 203, 21
Annibali F., Bressan A., Rampazzo R., Zeilinger W. W., Danese L., 2007, A&A, 463, 455
Arimoto N., Yoshii Y., 1987, A&A, 173, 23
Barton E. J., Bromley B. C., Geller M. J., 1999, ApJ, 511, L25
Beifiori A., Maraston C., Thomas D., Johansson J., 2011, A&A, 531, A109
Bekki K., Shioya Y., 1999, ApJ, 513, 108
Cappellari M., Emsellem E., 2004, PASP, 116, 138
Cole S., Lacey C. G., Baugh C. M., Frenk C. S., 2000, MNRAS, 319, 168
Corsini E. M., Méndez-Abreu J., Pastorello N., Dalla Bontà E., Morelli L., Beifiori A., Pizzella A., Bertola F., 2012, MNRAS, 423, L79
Creasey P., Theuns T., Bower R. G., 2013, MNRAS, 429, 1922
de Lorenzo-Cáceres A., Vazdekis A., Aguerri J. A. L., Corsini E. M., Debattista V. P., 2012, MNRAS, 420, 1092
De Lucia G., Kauffmann G., White S. D. M., 2004, MNRAS, 349, 1101
Denicoló G., Terlevich R., Terlevich E., Forbes D. A., Terlevich A., 2005, MNRAS, 358, 813

Di Matteo P., Pipino A., Lehnert M. D., Combes F., Semelin B., 2009, A&A, 499, 427

Eggen O. J., Lynden-Bell D., Sandage A. R., 1962, ApJ, 136, 748

Faber S. M., Friel E. D., Burstein D., Gaskell C. M., 1985, ApJS, 57, 711

Falcón-Barroso J., Sánchez-Blázquez P., Vazdekis A., Ricciardelli E., Cardiel N., Cenarro A. J., Gorgas J., Peletier R. F., 2011, A&A, 532, A95

Ferreras I., Silk J., 2002, MNRAS, 336, 1181

Ferrers N. M.1877, Q. J. Pure Appl. Math., 14, 1

Fisher D., Franx M., Illingworth G., 1996, ApJ, 459, 110

Freeman K. C., 1970, ApJ, 160, 811

Ganda K. et al., 2007, MNRAS, 380, 506

Gerhard O. E., 1993, MNRAS, 265, 213

Gilmore G., Wyse R. F. G., 1998, AJ, 116, 748

González Delgado R. M. et al., 2014, A&A, 562, A47

Gorgas J., Efstathiou G., Salamanca A. A., 1990, MNRAS, 245, 217

Hirschmann M., De Lucia G., Iovino A., Cucciati O., 2013, MNRAS, 433, 1479

Hirschmann M. et al., 2013, MNRAS, 436, 2929

Hirschmann M., Naab T., Ostriker J. P., Forbes D. A., Duc P.-A., Davé R., Oser L., Karabal E., 2015, MNRAS, 449, 528

Hopkins P. F., Cox T. J., Dutta S. N., Hernquist L., Kormendy J., Lauer T. R., 2009, ApJS, 181, 135

Idiart T. P., de Freitas Pacheco J. A., Costa R. D. D., 1996, AJ, 112, 2541

Jablonka P., Gorgas J., Goudfrooij P., 2007, A&A, 474, 763

James P. A., Percival S. M., 2016, MNRAS, 457, 917

Jedrzejewski R. I., 1987, MNRAS, 226, 747

Jørgensen I., 1999, MNRAS, 306, 607

Karachentseva V. E., 1973, Soobshch. Spets. Astrofiz. Obs., 8, 3

Katkov I. Y., Kniazev A. Y., Sil'chenko O. K., 2015, AJ, 150, 24

Kawata D., 2001, ApJ, 558, 598

Kawata D., Gibson B. K., 2003, MNRAS, 340, 908

Kobayashi C., 2004, MNRAS, 347, 740

Kobayashi C., Arimoto N., 1999, ApJ, 527, 573

Kodama T., Arimoto N., Barger A. J., Arag'on-Salamanca A., 1998, A&A, 334, 99

Kormendy J., Kennicutt R. C., 2004, ARA&A, 42, 603

Kuntschner H. et al., 2010, MNRAS, 408, 97

La Barbera F., Pasquali A., Ferreras I., Gallazzi A., de Carvalho R. R., de la Rosa I. G., 2014, MNRAS, 445, 1977

Larson R. B., 1974, MNRAS, 166, 585

McDermid R. M. et al., 2015, MNRAS, 448, 3484

Marinoni S., Galleti S., Cocozza G., Pancino E., Altavilla E., 2013, Technical Report, Instrument Familiarization Plan for Ground Based Observations of SPSS. II. Calibration Frames Study and Recommendations

Matteucci F., 1994, A&A, 288, 57

Matteucci F., Greggio L., 1986, A&A, 154, 279

Mehlert D., Thomas D., Saglia R. P., Bender R., Wegner G., 2003, A&A, 407, 423

Méndez-Abreu J., Aguerri J. A. L., Corsini E. M., Simonneau E., 2008, A&A, 478, 353

Méndez-Abreu J., Debattista V. P., Corsini E. M., Aguerri J. A. L., 2014, A&A, 572, A25

Moorthy B. K., Holtzman J. A., 2006, MNRAS, 371, 583

Morelli L. et al., 2004, MNRAS, 354, 753

Morelli L. et al., 2008, MNRAS, 389, 341

Morelli L., Cesetti M., Corsini E. M., Pizzella A., Dalla Bontà E., Sarzi M., Bertola F., 2010, A&A, 518, A32

Morelli L., Corsini E. M., Pizzella A., Dalla Bontà E., Coccato L., Méndez-Abreu J., Cesetti M., 2012, MNRAS, 423, 962

Morelli L., Pizzella A., Corsini E. M., Dalla Bontà E., Coccato L., Méndez-Abreu J., Parmiggiani M., 2015, Astron. Nachr., 336, 208

Morelli L., Corsini E. M., Pizzella A., Dalla Bontà E., Coccato L., Méndez-Abreu J., 2015, MNRAS, 452, 1128

Peletier R. F. et al., 2007, MNRAS, 379, 445

Pérez I., Sánchez-Blázquez P., 2011, A&A, 529, A64

Pipino A., D'Ercole A., Matteucci F., 2008, A&A, 484, 679

Pipino A., D'Ercole A., Chiappini C., Matteucci F., 2010, MNRAS, 407, 1347

Pizzella A., Corsini E. M., Sarzi M., Magorrian J., Méndez-Abreu J., Coccato L., Morelli L., Bertola F., 2008, MNRAS, 387, 1099

Proctor R. N., Sansom A. E., 2002, MNRAS, 333, 517

Prugniel P., Maubon G., Simien F., 2001, A&A, 366, 68

Rawle T. D., Smith R. J., Lucey J. R., 2010, MNRAS, 401, 852

Reda F. M., Proctor R. N., Forbes D. A., Hau G. K. T., Larsen S. S., 2007, MNRAS, 377, 1772

Sánchez-Blázquez P. et al., 2006, MNRAS, 371, 703

Sánchez-Blázquez P., Gorgas J., Cardiel N., González J. J., 2006, A&A, 457, 809

Sánchez-Blázquez P., Gorgas J., Cardiel N., 2006, A&A, 457, 823

Sánchez-Blázquez P., Ocvirk P., Gibson B. K., Pérez I., Peletier R. F., 2011, MNRAS, 415, 709

Sánchez-Blázquez P. et al., 2014, A&A, 570, A6

Sarzi M. et al., 2006, MNRAS, 366, 1151

Seidel M. K., Falcón-Barroso J., Martínez-Valpuesta I., Díaz-García S., Laurikainen E., Salo H., Knapen J. H., 2015, MNRAS, 451, 936

Seidel M. K., Falcón-Barroso J., Martínez-Valpuesta I., Sánchez-Blázquez P., Párez I., Peletier R., Vazdekis A., 2016, MNRAS, 460, 3784

Sérsic J. L., 1968, Atlas de Galaxias Australes. Observatorio Astronomico, Cordoba

Sil'chenko O. K., Proshina I. S., Shulga A. P., Koposov S. E., 2012, MNRAS, 427, 790

Spolaor M., Kobayashi C., Forbes D. A., Couch W. J., Hau G. K. T., 2010, MNRAS, 408, 272

Tassis K., Kravtsov A. V., Gnedin N. Y., 2008, ApJ, 672, 888

Thomas D., Davies R. L., 2006, MNRAS, 366, 510

Thomas D., Maraston C., Bender R., 2003, MNRAS, 339, 897

Thomas D., Maraston C., Bender R., Mendes de Oliveira C., 2005, ApJ, 621, 673

Thomas D., Maraston C., Schawinski K., Sarzi M., Silk J., 2010, MNRAS, 404, 1775

Trager S. C., Worthey G., Faber S. M., Burstein D., Gonzalez J. J., 1998, ApJS, 116, 1

van Albada T. S., 1982, MNRAS, 201, 939

van der Marel R. P., Franx M., 1993, ApJ, 407, 525

Vazdekis A., Sánchez-Blázquez P., Falcón-Barroso J., Cenarro A. J., Beasley M. A., Cardiel N., Gorgas J., Peletier R. F., 2010, MNRAS, 404, 1639

Wilkinson D. M. et al., 2015, MNRAS, 449, 328

Worthey G., Faber S. M., Gonzalez J. J., Burstein D., 1994, ApJS, 94, 687

Wozniak H., 2007, A&A, 465, L1

York D. G. et al., 2000, AJ, 120, 1579

APPENDIX A: PHOTOMETRIC DECOMPOSITION, STELLAR KINEMATIC AND LINE STRENGTH INDICES

The photometric decomposition of all the sample galaxies are plotted in Fig. A1. The stellar kinematics of all the sample galaxies are given in Table A1 and plotted in Fig. A2, respectively. The line-strength indices of all the sample galaxies are given in Table A1 too and plotted in Fig. A2.
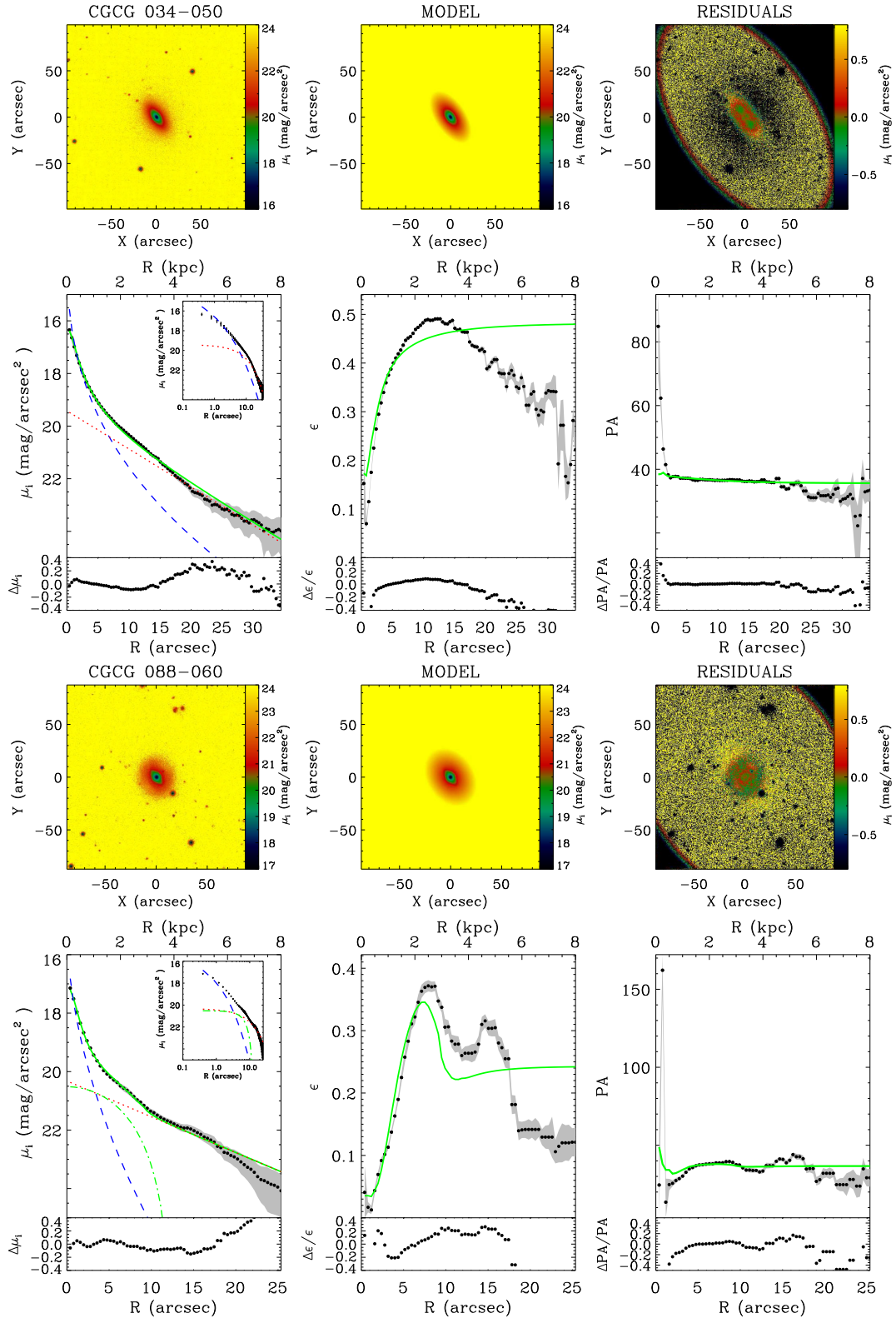
Figure A1. Two-dimensional photometric decomposition of the SDSS *i*-band images of the sample galaxies. Upper panels (from left- to right-hand side): map of the observed, modelled, and residual (observed-modelled) surface brightness distribution of the galaxy. The surface brightness range of each image is indicated at the right-hand side of the panel. In each panel, the spatial coordinates with respect to the galaxy centre are given in arcsec. Lower panels (from left- to right-hand side): ellipse-averaged radial profile of surface brightness, position angle, and ellipticity measured in the observed (black circles with error bars given as a grey area) and modelled image (green solid line). The radial profiles of the intrinsic surface brightness contribution of the bulge (blue dashed line), disc (red dotted line), and bar (green dash–dotted line) are given in the lower left panel with an inset showing the fit with a logarithmic scale for the distance to the galaxy centre. The difference between the ellipse-averaged radial profiles extracted from the observed and modelled images is also shown.
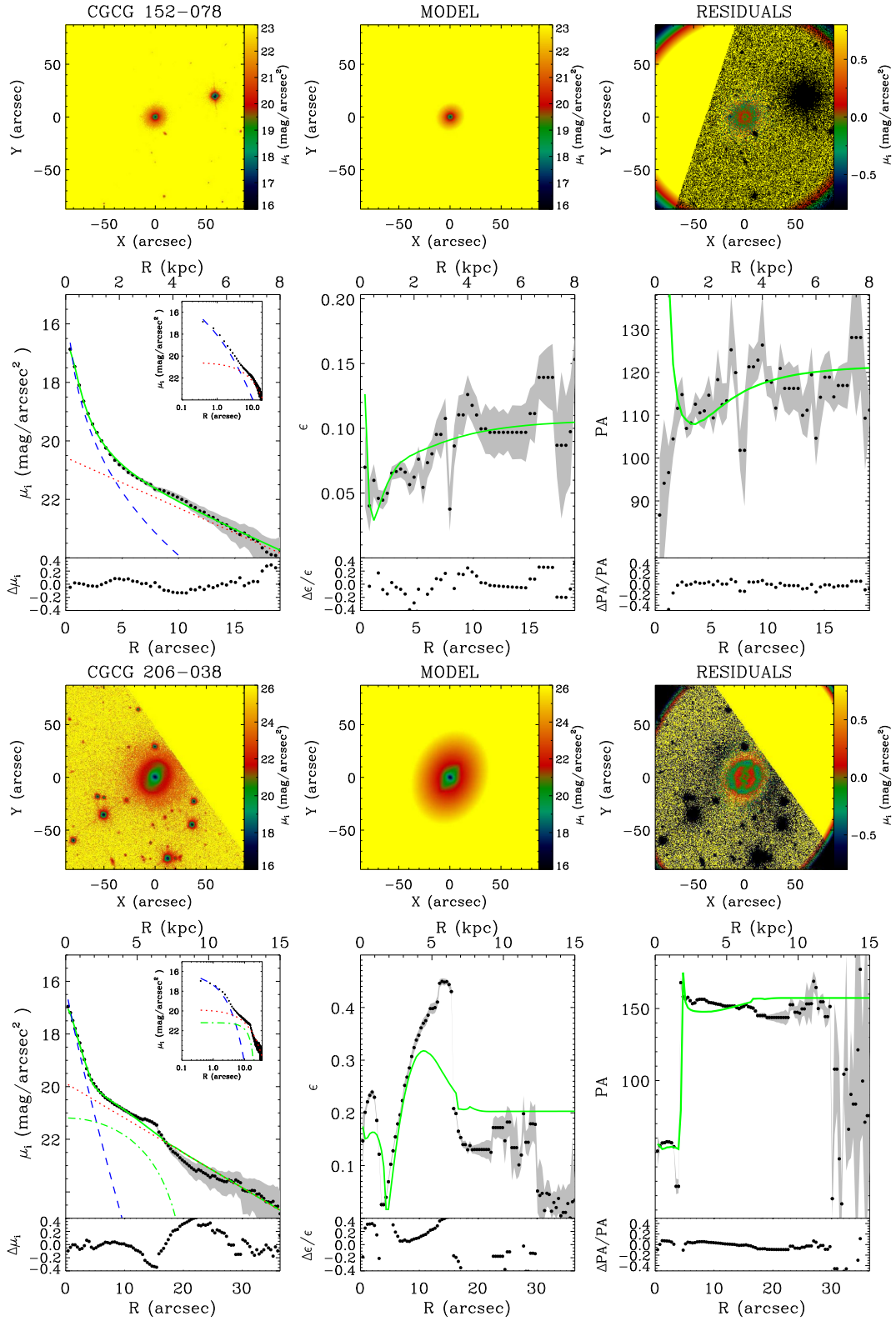
Figure A1 – *continued*
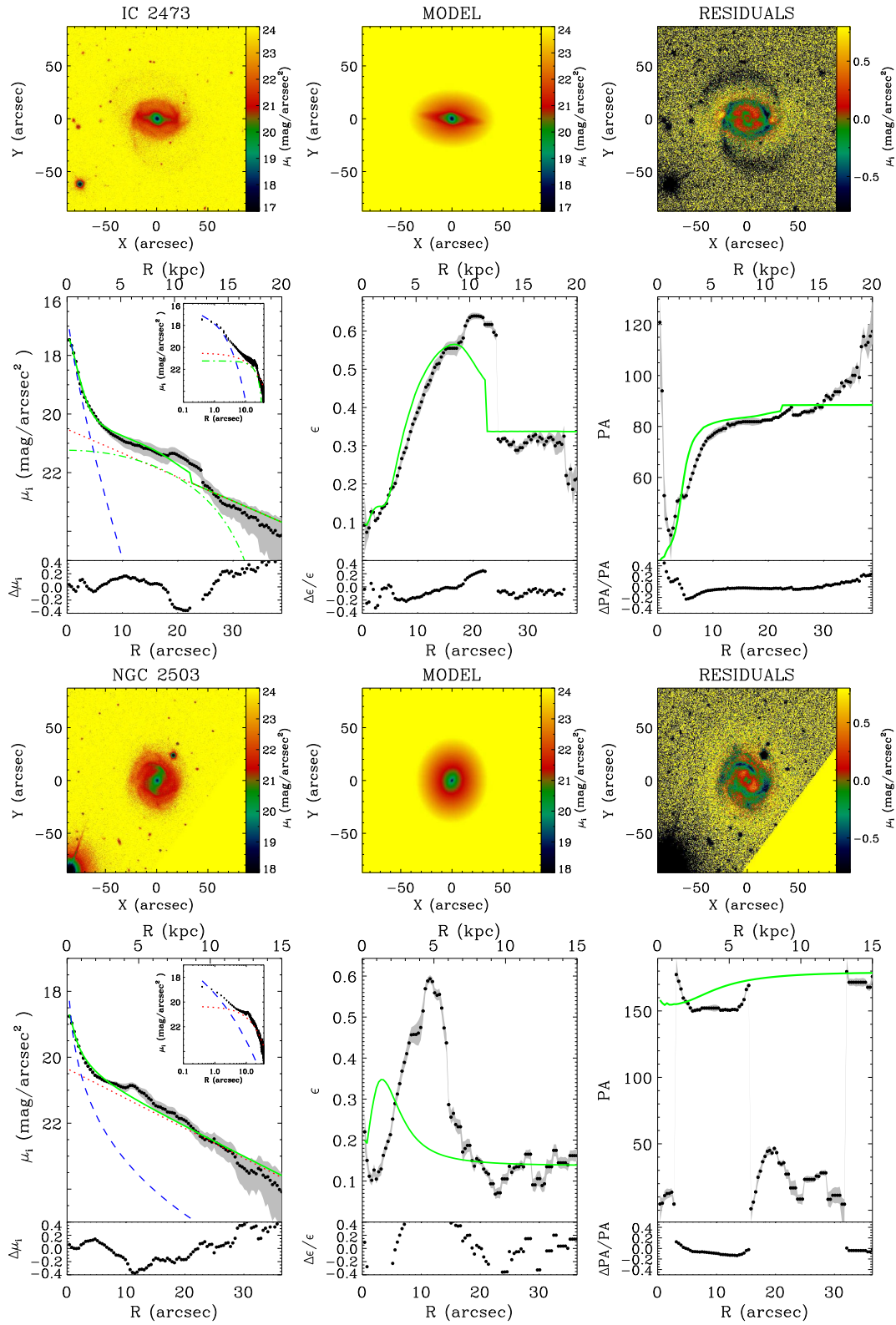
Figure A1 *– continued*
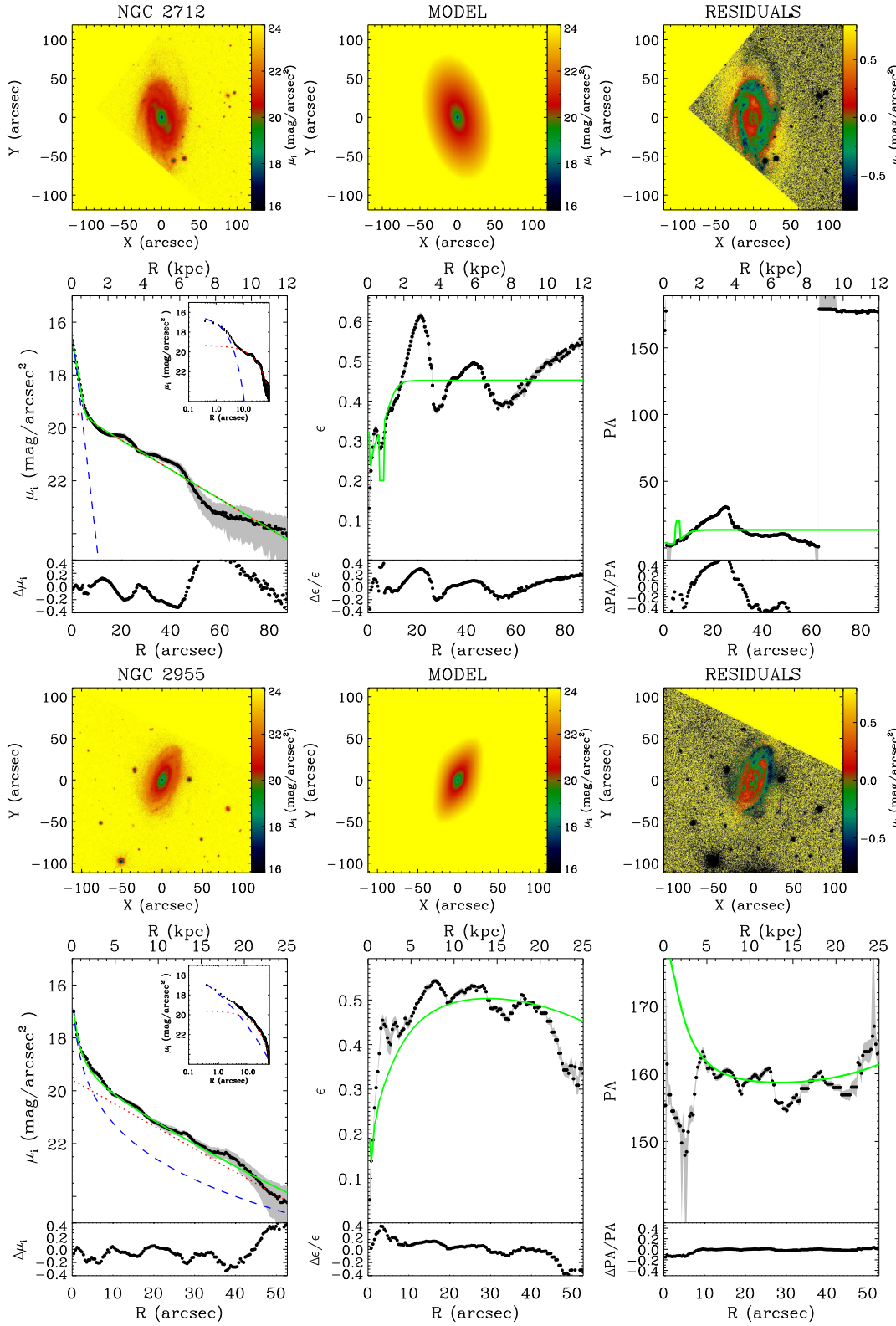
Figure A1 – *continued*
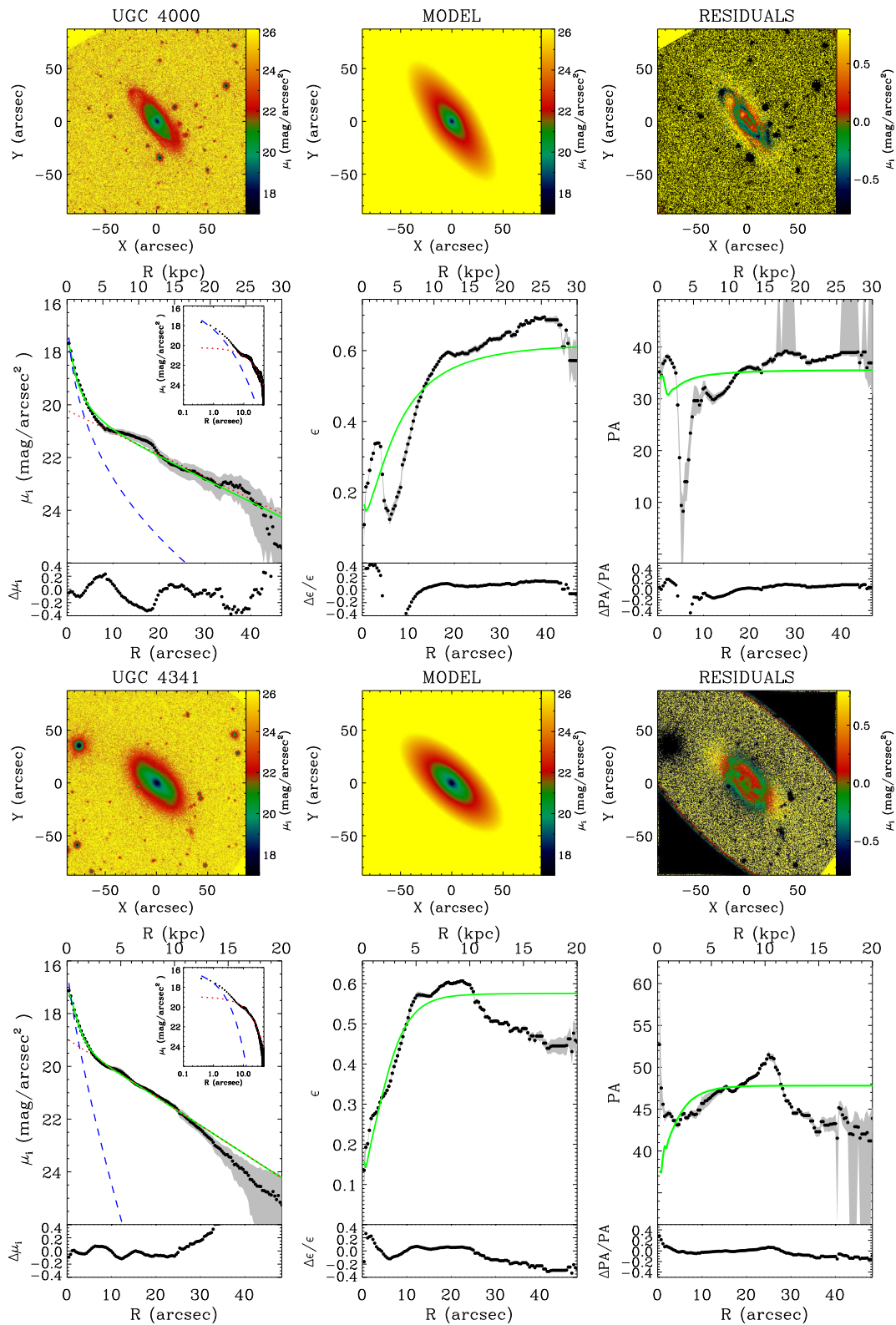
Figure A1 *– continued*
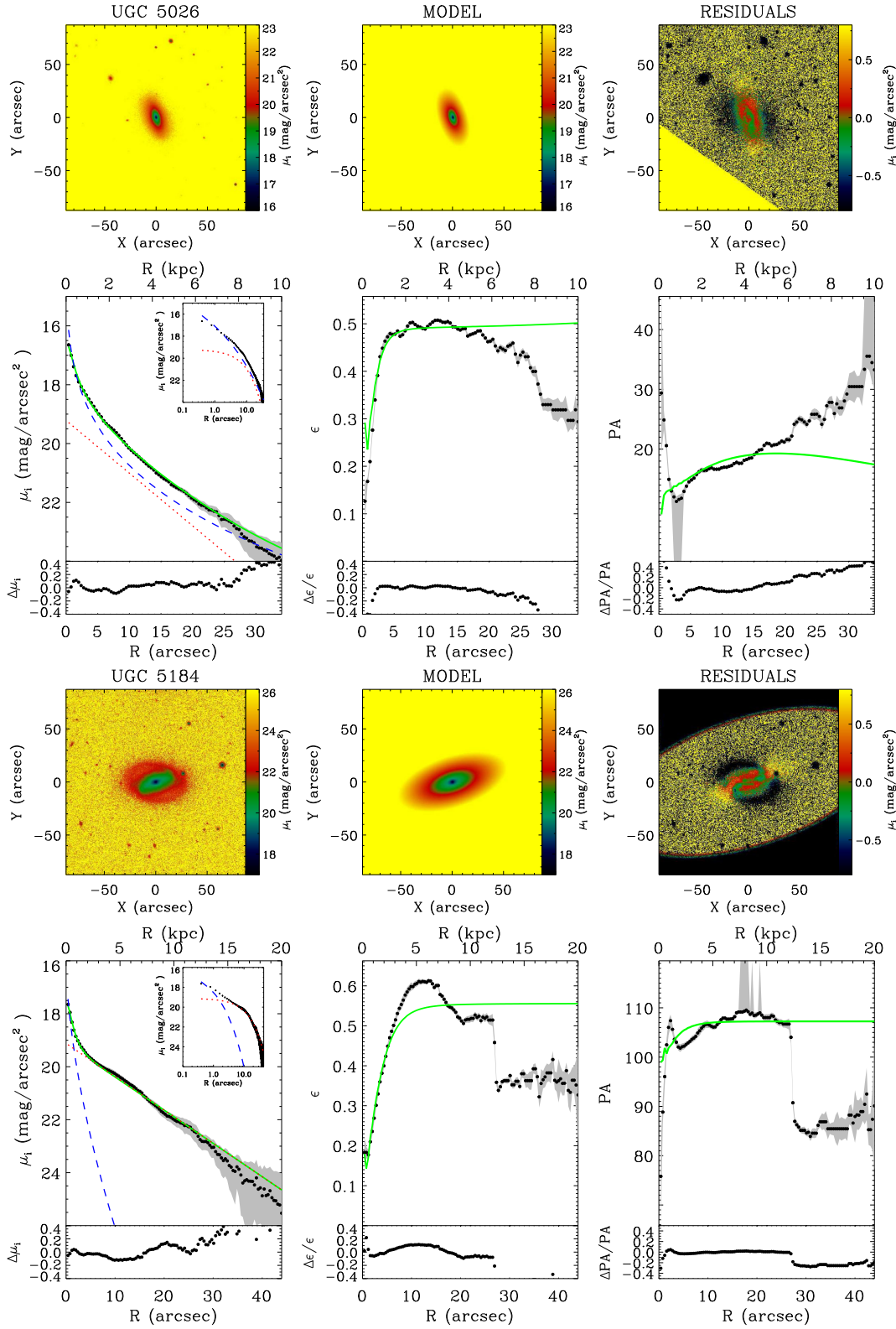
Figure A1 *– continued*

Table A1. Stellar kinematics and line-strength indices measured along the major axis of the sample galaxies. The columns show the following. (1): radius; (2): LOS velocity after subtraction of systemic velocity; (3): LOS velocity dispersion; (4): third-order Gauss–Hermite coefficient; (5): fourth-order Gauss–Hermite coefficient; (6)–(10): equivalent width of the line-strength indices.

| r (arcsec) (1)	v (km s^{-1}) (2)	σ (km s^{-1}) (3)	h_3 (4)	h_4 (5)	Hβ (Å) (6)	Mg$_2$ (mag) (7)	Mg$_b$ (Å) (8)	Fe5270 (Å) (9)	Fe5335 (Å) (10)
CGCG 034-050									
−19.28	−149.9 ± 19.8	112.6 ± 28.8	0.001 ± 0.090	0.015 ± 0.176	1.196 ± 0.592	0.043 ± 0.043	−1.802 ± 0.650	1.220 ± 0.691	3.270 ± 0.704
−7.41	−156.6 ± 4.7	85.7 ± 7.2	0.025 ± 0.045	0.107 ± 0.052	1.303 ± 0.154	0.220 ± 0.220	3.036 ± 0.198	2.389 ± 0.183	2.523 ± 0.174
−4.81	−145.6 ± 3.9	121.4 ± 5.9	0.019 ± 0.027	0.097 ± 0.031	1.569 ± 0.126	0.254 ± 0.254	3.699 ± 0.169	3.045 ± 0.154	2.146 ± 0.151
−3.48	−138.7 ± 3.8	122.3 ± 5.8	0.057 ± 0.025	0.107 ± 0.031	1.499 ± 0.111	0.256 ± 0.256	3.769 ± 0.158	2.521 ± 0.144	2.557 ± 0.133
−2.61	−118.5 ± 3.9	144.4 ± 5.7	0.086 ± 0.022	0.111 ± 0.027	1.533 ± 0.104	0.272 ± 0.272	4.090 ± 0.163	2.565 ± 0.136	2.322 ± 0.123
−1.99	−101.7 ± 4.3	171.4 ± 6.0	0.038 ± 0.021	0.098 ± 0.023	1.298 ± 0.104	0.281 ± 0.281	4.190 ± 0.166	2.559 ± 0.137	2.491 ± 0.128
−1.49	−78.6 ± 3.8	180.5 ± 4.8	0.048 ± 0.018	0.040 ± 0.019	1.460 ± 0.089	0.278 ± 0.278	4.294 ± 0.143	2.446 ± 0.124	2.668 ± 0.115
−0.98	−48.0 ± 3.6	201.2 ± 4.6	0.005 ± 0.015	0.043 ± 0.016	1.090 ± 0.082	0.288 ± 0.288	4.349 ± 0.127	2.898 ± 0.117	2.965 ± 0.106
−0.61	−32.2 ± 4.0	196.4 ± 5.0	−0.025 ± 0.017	0.039 ± 0.018	1.440 ± 0.094	0.299 ± 0.299	4.598 ± 0.139	3.041 ± 0.140	2.724 ± 0.123
−0.36	−17.2 ± 4.0	196.0 ± 5.3	−0.002 ± 0.017	0.061 ± 0.018	1.391 ± 0.095	0.295 ± 0.295	4.544 ± 0.133	2.652 ± 0.139	2.656 ± 0.127
−0.11	−2.2 ± 3.9	208.0 ± 5.0	−0.015 ± 0.016	0.056 ± 0.017	1.132 ± 0.091	0.299 ± 0.299	4.553 ± 0.132	2.928 ± 0.135	2.700 ± 0.125
0.14	6.5 ± 4.0	209.0 ± 5.0	−0.039 ± 0.016	0.041 ± 0.017	1.207 ± 0.090	0.298 ± 0.298	4.793 ± 0.140	2.734 ± 0.141	2.712 ± 0.120
0.40	30.3 ± 4.1	210.1 ± 5.1	−0.053 ± 0.016	0.037 ± 0.018	1.401 ± 0.089	0.300 ± 0.300	4.594 ± 0.137	2.833 ± 0.140	2.909 ± 0.128
0.65	43.9 ± 4.1	203.6 ± 5.2	−0.055 ± 0.016	0.051 ± 0.018	1.444 ± 0.091	0.300 ± 0.300	4.767 ± 0.135	3.122 ± 0.143	2.600 ± 0.123
1.02	58.8 ± 3.6	195.2 ± 4.4	−0.078 ± 0.015	0.025 ± 0.017	1.420 ± 0.079	0.296 ± 0.296	4.618 ± 0.118	2.813 ± 0.127	2.759 ± 0.103
1.52	80.1 ± 4.1	193.5 ± 5.2	−0.085 ± 0.017	0.034 ± 0.019	1.231 ± 0.094	0.282 ± 0.282	4.470 ± 0.131	2.742 ± 0.147	2.798 ± 0.126
2.03	92.8 ± 4.7	179.8 ± 6.0	−0.108 ± 0.021	0.060 ± 0.024	1.653 ± 0.114	0.290 ± 0.290	4.531 ± 0.149	2.605 ± 0.163	2.576 ± 0.148
2.64	117.3 ± 4.2	142.4 ± 5.7	−0.150 ± 0.023	0.116 ± 0.029	1.166 ± 0.119	0.280 ± 0.280	4.175 ± 0.143	2.979 ± 0.162	2.695 ± 0.148
3.62	143.8 ± 4.1	134.3 ± 5.6	−0.119 ± 0.023	0.103 ± 0.029	1.630 ± 0.106	0.262 ± 0.262	3.950 ± 0.137	2.459 ± 0.154	2.281 ± 0.145
5.21	152.0 ± 4.2	106.8 ± 5.6	−0.083 ± 0.030	0.029 ± 0.038	1.576 ± 0.149	0.257 ± 0.257	3.692 ± 0.161	2.290 ± 0.178	2.467 ± 0.169
8.43	176.2 ± 4.7	80.2 ± 7.4	−0.098 ± 0.042	0.057 ± 0.065	1.517 ± 0.187	0.229 ± 0.229	3.369 ± 0.192	1.997 ± 0.200	2.310 ± 0.195
22.57	87.2 ± 26.1	75.7 ± 28.2	−0.019 ± 0.290	−0.039 ± 0.155	1.070 ± 0.683	0.100 ± 0.100	−1.948 ± 0.721	−0.499 ± 0.787	3.579 ± 0.754
CGCG 088-060									
−17.02	79.5 ± 25.1	39.5 ± 41.8	0.007 ± 0.447	−0.001 ± 0.525	1.426 ± 0.478	0.068 ± 0.017	1.420 ± 0.617	2.470 ± 0.622	4.095 ± 0.612
−5.34	64.4 ± 4.3	65.4 ± 7.5	−0.072 ± 0.049	0.053 ± 0.076	1.589 ± 0.177	0.210 ± 0.006	3.389 ± 0.230	2.588 ± 0.210	2.905 ± 0.202
−3.00	42.9 ± 4.2	88.0 ± 5.8	−0.019 ± 0.039	0.039 ± 0.042	1.973 ± 0.160	0.212 ± 0.005	3.637 ± 0.209	2.142 ± 0.199	2.474 ± 0.181
−1.93	40.9 ± 4.0	94.5 ± 5.8	0.000 ± 0.035	0.049 ± 0.039	1.766 ± 0.152	0.209 ± 0.005	3.579 ± 0.191	2.480 ± 0.184	2.383 ± 0.163
−1.31	42.2 ± 3.7	104.1 ± 5.0	−0.099 ± 0.027	0.013 ± 0.036	1.908 ± 0.146	0.205 ± 0.005	3.139 ± 0.179	3.095 ± 0.169	2.865 ± 0.155
−0.81	28.8 ± 3.3	111.0 ± 4.8	−0.029 ± 0.024	0.059 ± 0.029	1.536 ± 0.130	0.221 ± 0.004	3.609 ± 0.152	2.943 ± 0.144	2.770 ± 0.137
−0.44	2.4 ± 3.0	108.5 ± 4.1	−0.018 ± 0.023	0.028 ± 0.026	1.790 ± 0.119	0.228 ± 0.004	3.453 ± 0.144	3.115 ± 0.140	2.729 ± 0.130
−0.19	−4.1 ± 2.8	108.5 ± 4.2	−0.002 ± 0.021	0.077 ± 0.026	1.899 ± 0.111	0.243 ± 0.004	4.043 ± 0.137	2.923 ± 0.133	3.037 ± 0.121
0.06	−8.0 ± 2.9	112.1 ± 4.4	−0.024 ± 0.021	0.086 ± 0.026	2.083 ± 0.110	0.248 ± 0.004	4.262 ± 0.146	3.009 ± 0.135	2.748 ± 0.120
0.31	−16.0 ± 3.1	116.8 ± 4.1	−0.022 ± 0.022	0.023 ± 0.025	2.099 ± 0.115	0.244 ± 0.004	3.948 ± 0.148	2.945 ± 0.143	2.654 ± 0.126
0.68	−28.3 ± 2.6	112.0 ± 3.5	0.011 ± 0.019	0.026 ± 0.022	1.886 ± 0.104	0.236 ± 0.004	3.692 ± 0.129	2.838 ± 0.125	2.784 ± 0.110
1.19	−37.0 ± 3.5	115.4 ± 5.2	−0.032 ± 0.025	0.067 ± 0.030	2.014 ± 0.133	0.227 ± 0.005	3.665 ± 0.161	2.971 ± 0.160	2.720 ± 0.147
1.80	−41.7 ± 3.4	99.8 ± 4.7	−0.030 ± 0.027	0.014 ± 0.034	1.956 ± 0.141	0.229 ± 0.005	3.778 ± 0.171	2.800 ± 0.167	2.501 ± 0.151
2.77	−50.0 ± 4.2	96.6 ± 5.7	−0.010 ± 0.036	0.024 ± 0.038	1.581 ± 0.168	0.204 ± 0.006	3.382 ± 0.201	2.672 ± 0.196	2.707 ± 0.178
4.87	−66.8 ± 5.0	74.1 ± 6.3	0.004 ± 0.057	0.014 ± 0.052	1.616 ± 0.195	0.214 ± 0.007	3.444 ± 0.231	1.898 ± 0.237	1.771 ± 0.197
17.95	−49.1 ± 16.2	58.4 ± 33.1	−0.029 ± 0.199	−0.018 ± 0.353	1.855 ± 0.508	0.155 ± 0.017	1.618 ± 0.633	1.560 ± 0.688	2.252 ± 0.566
CGCG 152-078									
−11.86	75.8 ± 22.7	83.4 ± 33.0	−0.015 ± 0.159	0.005 ± 0.242	1.068 ± 0.697	0.105 ± 0.028	−1.147 ± 0.825	1.683 ± 1.278	−0.497 ± 1.113
−2.70	49.9 ± 4.0	85.1 ± 6.3	−0.069 ± 0.036	0.049 ± 0.051	2.022 ± 0.109	0.215 ± 0.005	3.224 ± 0.150	2.877 ± 0.227	2.150 ± 0.187
−1.36	31.1 ± 3.3	108.6 ± 4.4	−0.069 ± 0.024	0.005 ± 0.029	1.826 ± 0.078	0.221 ± 0.004	3.692 ± 0.109	2.649 ± 0.170	2.308 ± 0.141
−0.76	13.1 ± 3.1	114.6 ± 4.3	−0.075 ± 0.021	0.046 ± 0.026	1.526 ± 0.073	0.242 ± 0.003	3.932 ± 0.094	3.073 ± 0.146	2.811 ± 0.119
−0.40	0.2 ± 3.0	127.8 ± 4.3	−0.086 ± 0.019	0.065 ± 0.023	1.876 ± 0.087	0.245 ± 0.004	4.107 ± 0.101	2.995 ± 0.143	2.588 ± 0.122
−0.15	−3.4 ± 2.7	132.4 ± 3.9	−0.052 ± 0.017	0.064 ± 0.020	1.936 ± 0.092	0.252 ± 0.004	4.200 ± 0.101	3.013 ± 0.137	2.438 ± 0.117
0.11	−18.3 ± 2.9	131.9 ± 4.0	−0.005 ± 0.018	0.046 ± 0.020	1.981 ± 0.114	0.245 ± 0.004	4.073 ± 0.111	3.100 ± 0.146	2.852 ± 0.124
0.46	−26.1 ± 3.2	124.8 ± 4.6	0.030 ± 0.022	0.053 ± 0.025	2.021 ± 0.132	0.246 ± 0.005	4.057 ± 0.122	2.793 ± 0.165	2.686 ± 0.142
1.16	−45.5 ± 3.3	106.2 ± 4.8	0.002 ± 0.025	0.065 ± 0.029	1.816 ± 0.138	0.236 ± 0.005	3.912 ± 0.135	3.023 ± 0.186	2.555 ± 0.163
9.37	−77.3 ± 12.0	70.6 ± 14.8	−0.011 ± 0.129	0.031 ± 0.112	1.355 ± 0.364	0.177 ± 0.016	1.793 ± 0.427	1.621 ± 0.636	1.493 ± 0.584
CGCG 206-038									
−19.30	15.0 ± 21.1	58.7 ± 31.3	−0.021 ± 0.265	−0.005 ± 0.296	−0.762 ± 0.674	0.070 ± 0.028	2.916 ± 0.772	4.110 ± 0.932	2.796 ± 0.951
−6.75	16.6 ± 5.8	128.6 ± 7.9	0.045 ± 0.035	0.012 ± 0.043	1.913 ± 0.168	0.232 ± 0.008	3.558 ± 0.227	2.370 ± 0.243	2.624 ± 0.252
−3.22	8.9 ± 4.7	157.3 ± 6.3	−0.029 ± 0.025	0.046 ± 0.027	1.783 ± 0.114	0.261 ± 0.005	4.294 ± 0.151	3.228 ± 0.170	2.318 ± 0.184
−2.06	24.7 ± 4.0	147.2 ± 6.1	−0.049 ± 0.023	0.124 ± 0.028	1.264 ± 0.096	0.265 ± 0.005	3.683 ± 0.128	3.511 ± 0.149	2.826 ± 0.162
−1.44	6.5 ± 4.2	170.6 ± 5.6	−0.010 ± 0.021	0.050 ± 0.022	1.505 ± 0.098	0.272 ± 0.005	4.072 ± 0.130	2.965 ± 0.149	2.710 ± 0.165
−0.94	11.1 ± 3.4	179.6 ± 4.8	0.001 ± 0.016	0.086 ± 0.018	1.248 ± 0.085	0.279 ± 0.004	4.623 ± 0.108	3.186 ± 0.125	2.680 ± 0.137
−0.58	9.6 ± 3.7	184.8 ± 5.1	−0.006 ± 0.017	0.069 ± 0.019	1.127 ± 0.100	0.285 ± 0.004	4.644 ± 0.123	3.239 ± 0.142	3.203 ± 0.148
−0.32	0.6 ± 3.7	188.5 ± 4.9	−0.038 ± 0.017	0.052 ± 0.018	1.357 ± 0.104	0.278 ± 0.004	4.771 ± 0.140	3.386 ± 0.132	3.496 ± 0.149
−0.07	−7.9 ± 3.7	184.9 ± 5.1	0.004 ± 0.017	0.074 ± 0.019	1.352 ± 0.115	0.290 ± 0.004	4.791 ± 0.144	3.093 ± 0.131	2.837 ± 0.146
0.18	−4.8 ± 3.6	179.6 ± 5.1	0.007 ± 0.017	0.093 ± 0.019	1.357 ± 0.117	0.295 ± 0.004	4.796 ± 0.145	3.243 ± 0.126	3.224 ± 0.146
0.43	−5.6 ± 3.9	192.0 ± 5.4	−0.012 ± 0.017	0.082 ± 0.019	1.259 ± 0.128	0.298 ± 0.005	4.740 ± 0.159	3.476 ± 0.137	3.417 ± 0.168
0.80	−7.4 ± 4.0	183.4 ± 5.6	−0.008 ± 0.019	0.081 ± 0.021	1.365 ± 0.135	0.295 ± 0.005	4.669 ± 0.168	3.132 ± 0.136	3.043 ± 0.165
1.40	−14.6 ± 4.3	168.8 ± 5.9	0.022 ± 0.022	0.069 ± 0.024	1.481 ± 0.144	0.267 ± 0.006	4.277 ± 0.171	2.775 ± 0.147	2.698 ± 0.169
2.38	−17.3 ± 4.8	136.2 ± 7.2	0.014 ± 0.029	0.167 ± 0.035	1.329 ± 0.163	0.263 ± 0.006	4.080 ± 0.189	2.876 ± 0.166	2.521 ± 0.191

Table A1 – *continued*

r (arcsec) (1)	v (km s⁻¹) (2)	σ (km s⁻¹) (3)	h_3 (4)	h_4 (5)	Hβ (Å) (6)	Mg₂ (mag) (7)	Mg$_b$ (Å) (8)	Fe5270 (Å) (9)	Fe5335 (Å) (10)
4.54	−16.5 ± 5.8	144.7 ± 7.6	0.001 ± 0.035	0.030 ± 0.034	1.486 ± 0.184	0.264 ± 0.007	4.280 ± 0.224	2.272 ± 0.206	2.306 ± 0.232
16.39	−18.0 ± 14.7	75.0 ± 16.4	0.003 ± 0.151	−0.043 ± 0.117	0.605 ± 0.427	0.171 ± 0.018	3.111 ± 0.527	2.308 ± 0.503	2.109 ± 0.591
IC 2473									
−29.42	−133.6 ± 37.6	153.7 ± 39.6	0.024 ± 0.206	0.005 ± 0.065	2.352 ± 0.916	0.057 ± 0.034	0.770 ± 1.353	2.093 ± 1.367	1.121 ± 1.798
−16.38	−65.2 ± 10.7	89.0 ± 12.5	0.018 ± 0.100	0.018 ± 0.067	2.710 ± 0.285	0.202 ± 0.011	3.200 ± 0.391	1.719 ± 0.412	0.661 ± 0.501
−8.24	−25.4 ± 9.3	113.2 ± 12.8	−0.048 ± 0.052	−0.007 ± 0.083	0.866 ± 0.285	0.199 ± 0.010	2.603 ± 0.362	3.015 ± 0.351	1.288 ± 0.438
−4.43	−24.2 ± 8.2	125.0 ± 11.3	−0.080 ± 0.045	0.003 ± 0.066	2.640 ± 0.251	0.178 ± 0.008	3.821 ± 0.315	1.442 ± 0.328	2.039 ± 0.388
−2.98	−37.1 ± 9.0	136.2 ± 11.9	0.026 ± 0.050	0.020 ± 0.058	2.376 ± 0.243	0.166 ± 0.008	2.698 ± 0.305	3.781 ± 0.327	2.960 ± 0.373
−2.12	−0.6 ± 8.0	134.1 ± 10.8	−0.042 ± 0.042	−0.016 ± 0.061	3.077 ± 0.211	0.166 ± 0.007	2.496 ± 0.257	2.277 ± 0.309	1.827 ± 0.315
−1.50	−8.8 ± 7.7	121.6 ± 10.7	−0.030 ± 0.045	0.012 ± 0.064	1.857 ± 0.198	0.145 ± 0.006	2.783 ± 0.251	2.167 ± 0.286	2.290 ± 0.287
−1.00	−2.9 ± 7.4	132.5 ± 10.0	−0.033 ± 0.046	0.036 ± 0.047	2.054 ± 0.177	0.132 ± 0.005	2.145 ± 0.221	1.968 ± 0.246	1.336 ± 0.262
−0.62	−1.1 ± 9.6	135.5 ± 13.1	−0.074 ± 0.047	0.031 ± 0.068	1.542 ± 0.220	0.140 ± 0.006	2.799 ± 0.279	1.128 ± 0.302	1.875 ± 0.306
−0.37	25.9 ± 9.3	128.2 ± 12.4	−0.100 ± 0.046	−0.000 ± 0.071	1.446 ± 0.216	0.120 ± 0.006	2.879 ± 0.250	1.012 ± 0.308	2.154 ± 0.297
−0.12	17.4 ± 8.8	129.8 ± 12.3	−0.071 ± 0.052	0.049 ± 0.058	1.751 ± 0.215	0.134 ± 0.006	1.789 ± 0.246	1.781 ± 0.300	1.880 ± 0.304
0.13	40.2 ± 8.9	123.3 ± 12.2	−0.027 ± 0.047	0.016 ± 0.072	2.195 ± 0.222	0.122 ± 0.006	2.514 ± 0.227	1.867 ± 0.300	1.120 ± 0.309
0.38	29.8 ± 10.3	142.6 ± 13.1	−0.126 ± 0.045	0.011 ± 0.067	1.775 ± 0.227	0.143 ± 0.006	2.856 ± 0.252	1.677 ± 0.309	2.190 ± 0.309
0.64	35.9 ± 9.4	141.6 ± 12.7	−0.124 ± 0.044	0.046 ± 0.063	1.382 ± 0.214	0.133 ± 0.007	1.929 ± 0.261	1.898 ± 0.317	2.577 ± 0.325
1.01	42.1 ± 7.4	135.2 ± 9.5	−0.096 ± 0.038	0.015 ± 0.051	1.969 ± 0.182	0.137 ± 0.006	2.561 ± 0.217	1.799 ± 0.266	1.852 ± 0.279
1.51	27.1 ± 8.7	133.7 ± 10.8	0.023 ± 0.049	−0.019 ± 0.056	1.730 ± 0.211	0.157 ± 0.007	2.658 ± 0.254	2.213 ± 0.321	1.941 ± 0.326
2.13	28.8 ± 8.6	139.7 ± 11.3	−0.025 ± 0.047	0.024 ± 0.051	2.227 ± 0.200	0.160 ± 0.006	2.647 ± 0.242	2.198 ± 0.302	1.861 ± 0.307
3.00	12.3 ± 9.2	136.1 ± 12.2	−0.069 ± 0.044	0.030 ± 0.064	1.697 ± 0.232	0.182 ± 0.008	3.273 ± 0.280	2.525 ± 0.372	2.354 ± 0.354
4.24	24.2 ± 9.4	138.2 ± 13.0	−0.082 ± 0.048	0.065 ± 0.048	1.047 ± 0.241	0.208 ± 0.008	2.919 ± 0.303	3.229 ± 0.411	2.744 ± 0.380
6.35	3.0 ± 9.4	153.5 ± 10.7	−0.076 ± 0.047	−0.028 ± 0.051	2.159 ± 0.253	0.204 ± 0.009	3.093 ± 0.319	3.363 ± 0.442	2.348 ± 0.392
9.88	−11.9 ± 9.0	121.7 ± 9.6	−0.051 ± 0.060	−0.068 ± 0.056	2.047 ± 0.252	0.226 ± 0.009	3.401 ± 0.349	3.493 ± 0.467	1.568 ± 0.408
15.57	16.4 ± 8.0	89.3 ± 12.7	−0.021 ± 0.057	−0.007 ± 0.103	2.824 ± 0.272	0.209 ± 0.010	2.311 ± 0.335	2.182 ± 0.490	0.710 ± 0.420
27.16	6.6 ± 32.5	124.9 ± 49.9	−0.027 ± 0.097	−0.008 ± 0.284	3.163 ± 0.751	0.176 ± 0.030	0.830 ± 1.048	2.781 ± 1.641	1.941 ± 1.470
NGC 2503									
−23.50	119.2 ± 17.2	65.7 ± 17.8	0.013 ± 0.208	−0.010 ± 0.114	2.873 ± 0.455	0.024 ± 0.015	1.011 ± 0.541	1.349 ± 0.707	1.231 ± 0.634
−9.59	82.3 ± 9.2	75.5 ± 10.4	−0.010 ± 0.097	0.046 ± 0.060	2.465 ± 0.309	0.166 ± 0.010	1.916 ± 0.356	3.326 ± 0.447	1.619 ± 0.373
−4.58	56.6 ± 6.6	77.4 ± 12.1	−0.030 ± 0.053	−0.006 ± 0.113	1.569 ± 0.286	0.182 ± 0.010	2.420 ± 0.319	1.708 ± 0.411	2.096 ± 0.348
−2.55	45.3 ± 6.4	69.9 ± 11.9	−0.037 ± 0.059	−0.012 ± 0.121	2.457 ± 0.259	0.167 ± 0.009	1.779 ± 0.297	2.963 ± 0.381	2.020 ± 0.320
−1.57	37.0 ± 6.7	77.6 ± 7.5	0.007 ± 0.070	−0.043 ± 0.057	2.713 ± 0.243	0.155 ± 0.008	2.603 ± 0.267	3.138 ± 0.323	1.988 ± 0.311
−0.95	18.3 ± 6.3	77.6 ± 9.7	0.056 ± 0.061	0.051 ± 0.079	2.967 ± 0.253	0.175 ± 0.008	2.959 ± 0.257	1.803 ± 0.321	2.793 ± 0.304
−0.45	8.5 ± 6.0	65.7 ± 8.1	−0.014 ± 0.072	0.050 ± 0.071	2.177 ± 0.212	0.162 ± 0.007	3.406 ± 0.209	2.709 ± 0.261	2.268 ± 0.253
−0.07	−1.8 ± 7.7	86.1 ± 10.0	0.016 ± 0.073	0.079 ± 0.058	2.548 ± 0.248	0.161 ± 0.008	3.261 ± 0.245	2.029 ± 0.309	2.188 ± 0.310
0.18	−12.1 ± 7.4	95.3 ± 9.7	−0.033 ± 0.063	0.030 ± 0.057	2.320 ± 0.245	0.168 ± 0.007	3.336 ± 0.255	1.426 ± 0.306	1.519 ± 0.303
0.55	−27.3 ± 5.3	73.2 ± 8.5	0.053 ± 0.055	0.028 ± 0.076	2.244 ± 0.206	0.165 ± 0.006	2.942 ± 0.199	2.756 ± 0.266	2.527 ± 0.245
1.05	−22.8 ± 6.3	69.9 ± 8.5	0.004 ± 0.072	−0.009 ± 0.076	2.656 ± 0.232	0.162 ± 0.007	2.466 ± 0.249	3.044 ± 0.305	2.149 ± 0.287
1.67	−41.8 ± 6.6	77.8 ± 8.8	−0.074 ± 0.061	−0.026 ± 0.081	1.678 ± 0.239	0.179 ± 0.007	2.699 ± 0.265	2.449 ± 0.321	2.448 ± 0.309
2.66	−35.0 ± 7.1	79.4 ± 9.9	−0.030 ± 0.070	0.034 ± 0.077	2.004 ± 0.258	0.187 ± 0.008	2.736 ± 0.289	2.605 ± 0.367	2.461 ± 0.340
4.60	−50.9 ± 6.7	72.6 ± 13.5	0.017 ± 0.055	−0.016 ± 0.133	1.959 ± 0.271	0.199 ± 0.008	3.818 ± 0.303	2.799 ± 0.410	2.034 ± 0.382
9.09	−79.1 ± 7.9	63.1 ± 13.2	0.036 ± 0.090	0.026 ± 0.131	1.443 ± 0.255	0.165 ± 0.008	2.356 ± 0.313	0.885 ± 0.449	1.991 ± 0.402
21.87	−95.7 ± 19.7	41.2 ± 51.1	−0.008 ± 0.309	0.005 ± 0.657	2.160 ± 0.382	0.156 ± 0.014	3.031 ± 0.542	2.270 ± 0.800	1.878 ± 0.686
NGC 2712									
−35.77	−140.1 ± 24.8	35.1 ± 28.4	0.008 ± 0.471	0.008 ± 0.471	3.067 ± 0.311	0.094 ± 0.009	2.209 ± 0.385	1.907 ± 0.439	1.529 ± 0.442
−26.96	−137.8 ± 6.6	56.3 ± 19.8	0.044 ± 0.063	−0.001 ± 0.231	4.030 ± 0.261	0.113 ± 0.008	2.719 ± 0.322	1.225 ± 0.377	0.271 ± 0.356
−20.76	−120.2 ± 9.0	74.6 ± 9.8	0.074 ± 0.097	−0.073 ± 0.083	2.462 ± 0.266	0.108 ± 0.008	2.480 ± 0.322	1.787 ± 0.370	1.174 ± 0.360
−15.88	−92.4 ± 7.2	86.0 ± 11.0	0.101 ± 0.052	−0.010 ± 0.097	2.301 ± 0.240	0.137 ± 0.008	2.961 ± 0.318	2.106 ± 0.347	0.880 ± 0.346
−11.96	−84.1 ± 7.3	96.8 ± 9.7	0.016 ± 0.058	0.035 ± 0.060	2.077 ± 0.232	0.169 ± 0.008	2.746 ± 0.320	2.689 ± 0.321	1.152 ± 0.330
−8.95	−51.7 ± 6.2	108.2 ± 8.6	−0.021 ± 0.041	−0.008 ± 0.045	1.135 ± 0.212	0.175 ± 0.007	3.147 ± 0.293	2.510 ± 0.291	1.815 ± 0.297
−6.82	−44.5 ± 5.8	96.3 ± 6.4	−0.009 ± 0.051	−0.037 ± 0.043	2.112 ± 0.181	0.151 ± 0.006	1.965 ± 0.254	2.187 ± 0.244	2.028 ± 0.251
−5.32	−42.1 ± 5.3	99.8 ± 6.5	0.005 ± 0.043	−0.022 ± 0.045	2.273 ± 0.163	0.162 ± 0.006	2.953 ± 0.233	2.081 ± 0.220	1.771 ± 0.247
−4.19	−37.8 ± 4.9	100.9 ± 6.7	0.064 ± 0.036	−0.013 ± 0.050	2.875 ± 0.135	0.163 ± 0.005	2.855 ± 0.207	2.285 ± 0.194	1.481 ± 0.223
−3.32	−33.8 ± 5.0	101.1 ± 6.8	0.065 ± 0.035	0.031 ± 0.047	1.894 ± 0.132	0.160 ± 0.005	3.200 ± 0.199	2.162 ± 0.185	2.071 ± 0.211
−2.70	−28.6 ± 4.8	100.6 ± 6.7	0.024 ± 0.038	0.053 ± 0.042	2.437 ± 0.130	0.155 ± 0.005	3.073 ± 0.203	2.489 ± 0.176	2.167 ± 0.211
−2.19	−18.2 ± 4.6	90.5 ± 6.9	0.038 ± 0.041	0.078 ± 0.048	2.755 ± 0.124	0.152 ± 0.005	2.612 ± 0.193	2.174 ± 0.166	2.238 ± 0.199
−1.69	−15.6 ± 4.1	91.8 ± 6.0	−0.042 ± 0.035	0.092 ± 0.043	2.276 ± 0.118	0.151 ± 0.004	2.877 ± 0.183	2.496 ± 0.158	2.196 ± 0.187
−1.19	−13.9 ± 3.6	89.2 ± 5.0	−0.016 ± 0.032	−0.020 ± 0.043	2.586 ± 0.117	0.151 ± 0.004	2.767 ± 0.170	1.862 ± 0.143	1.764 ± 0.175
−0.68	−8.2 ± 3.5	89.0 ± 4.8	−0.010 ± 0.029	0.011 ± 0.040	2.837 ± 0.115	0.160 ± 0.004	2.778 ± 0.161	2.126 ± 0.135	1.651 ± 0.163
−0.18	0.3 ± 3.6	92.8 ± 5.1	0.026 ± 0.030	0.038 ± 0.038	2.230 ± 0.116	0.157 ± 0.004	2.949 ± 0.162	2.278 ± 0.138	1.934 ± 0.159
0.32	3.8 ± 3.7	98.2 ± 4.9	−0.002 ± 0.031	0.021 ± 0.034	2.359 ± 0.116	0.165 ± 0.004	3.157 ± 0.171	2.496 ± 0.149	2.273 ± 0.174
0.82	17.7 ± 4.0	100.3 ± 4.5	0.015 ± 0.033	−0.035 ± 0.033	2.388 ± 0.122	0.158 ± 0.004	3.030 ± 0.176	2.103 ± 0.154	1.851 ± 0.180
1.33	17.7 ± 4.4	100.3 ± 5.2	−0.010 ± 0.037	−0.027 ± 0.036	2.707 ± 0.140	0.151 ± 0.005	2.844 ± 0.192	2.153 ± 0.177	2.195 ± 0.201
1.83	24.1 ± 5.0	93.1 ± 6.8	0.004 ± 0.043	0.061 ± 0.044	2.326 ± 0.146	0.147 ± 0.005	2.671 ± 0.200	2.268 ± 0.181	2.042 ± 0.207
2.33	35.2 ± 5.1	88.3 ± 7.6	−0.066 ± 0.040	0.036 ± 0.062	1.803 ± 0.164	0.146 ± 0.005	2.542 ± 0.223	2.341 ± 0.202	1.835 ± 0.233
2.84	42.7 ± 6.2	101.9 ± 8.6	−0.026 ± 0.046	0.033 ± 0.055	1.451 ± 0.197	0.138 ± 0.005	2.596 ± 0.244	2.164 ± 0.227	1.651 ± 0.263
3.46	40.2 ± 6.0	111.2 ± 7.9	−0.121 ± 0.037	0.046 ± 0.051	1.689 ± 0.181	0.159 ± 0.005	2.711 ± 0.225	2.539 ± 0.211	1.703 ± 0.246
4.33	38.7 ± 6.4	108.2 ± 7.2	−0.027 ± 0.048	−0.026 ± 0.046	2.452 ± 0.200	0.158 ± 0.005	2.695 ± 0.242	2.140 ± 0.211	1.720 ± 0.266
5.46	50.5 ± 6.1	80.0 ± 8.1	−0.013 ± 0.062	0.066 ± 0.056	2.015 ± 0.217	0.158 ± 0.006	2.782 ± 0.258	2.525 ± 0.229	2.484 ± 0.284

Table A1 – *continued*

r (arcsec) (1)	v (km s⁻¹) (2)	σ (km s⁻¹) (3)	h₃ (4)	h₄ (5)	Hβ (Å) (6)	Mg₂ (mag) (7)	Mgₐ (Å) (8)	Fe5270 (Å) (9)	Fe5335 (Å) (10)
6.96	44.3 ± 6.6	96.7 ± 9.4	−0.094 ± 0.048	0.067 ± 0.065	1.661 ± 0.225	0.168 ± 0.007	2.843 ± 0.278	2.065 ± 0.253	2.331 ± 0.304
9.09	72.1 ± 6.2	97.3 ± 8.7	−0.065 ± 0.043	0.021 ± 0.065	1.902 ± 0.218	0.177 ± 0.008	3.135 ± 0.286	2.542 ± 0.266	1.622 ± 0.308
12.20	89.3 ± 7.3	79.6 ± 9.1	0.032 ± 0.074	0.026 ± 0.062	2.200 ± 0.230	0.160 ± 0.008	3.007 ± 0.306	2.485 ± 0.278	2.455 ± 0.336
17.03	112.7 ± 7.8	77.2 ± 11.4	−0.022 ± 0.070	−0.008 ± 0.105	2.050 ± 0.266	0.153 ± 0.009	3.077 ± 0.356	2.190 ± 0.306	1.389 ± 0.385
24.42	130.3 ± 7.7	60.9 ± 19.2	0.046 ± 0.063	−0.000 ± 0.216	2.471 ± 0.292	0.124 ± 0.011	2.222 ± 0.390	1.872 ± 0.336	0.537 ± 0.420
33.10	142.7 ± 7.7	46.6 ± 39.9	0.027 ± 0.073	−0.004 ± 0.500	4.212 ± 0.283	0.098 ± 0.011	1.878 ± 0.393	1.142 ± 0.352	2.139 ± 0.389
NGC 2955									
−18.83	−187.0 ± 11.0	85.5 ± 14.1	0.019 ± 0.101	0.013 ± 0.090	3.646 ± 0.272	0.102 ± 0.010	1.959 ± 0.337	3.067 ± 0.367	2.514 ± 0.493
−14.19	−182.4 ± 11.3	99.7 ± 14.6	0.036 ± 0.091	0.019 ± 0.078	4.043 ± 0.250	0.100 ± 0.009	2.093 ± 0.305	2.347 ± 0.338	2.049 ± 0.453
−11.16	−158.6 ± 9.7	117.0 ± 14.1	0.053 ± 0.050	0.005 ± 0.088	3.805 ± 0.235	0.124 ± 0.009	2.479 ± 0.296	2.043 ± 0.315	2.467 ± 0.409
−8.89	−155.3 ± 9.6	115.2 ± 13.9	0.100 ± 0.055	0.037 ± 0.082	3.776 ± 0.222	0.108 ± 0.008	2.270 ± 0.277	2.174 ± 0.302	2.529 ± 0.392
−7.40	−130.0 ± 8.8	97.8 ± 13.8	0.029 ± 0.053	0.006 ± 0.102	3.199 ± 0.197	0.097 ± 0.008	1.895 ± 0.243	1.143 ± 0.273	1.513 ± 0.354
−6.28	−131.7 ± 8.5	102.6 ± 12.8	0.064 ± 0.053	0.015 ± 0.015	3.166 ± 0.194	0.109 ± 0.007	2.236 ± 0.236	1.269 ± 0.266	1.749 ± 0.347
−5.27	−120.0 ± 10.0	128.2 ± 10.7	0.015 ± 0.069	−0.031 ± −0.031	3.168 ± 0.182	0.112 ± 0.007	2.206 ± 0.228	1.090 ± 0.252	1.346 ± 0.333
−4.39	−106.3 ± 8.7	117.8 ± 11.0	0.007 ± 0.063	0.029 ± 0.029	3.339 ± 0.189	0.138 ± 0.007	2.724 ± 0.244	1.884 ± 0.265	1.490 ± 0.347
−3.63	−81.8 ± 7.6	112.0 ± 10.0	−0.024 ± 0.055	0.081 ± 0.081	2.830 ± 0.165	0.140 ± 0.006	2.889 ± 0.220	2.531 ± 0.237	2.060 ± 0.298
−3.01	−81.8 ± 8.6	131.1 ± 10.4	0.004 ± 0.056	0.007 ± 0.007	3.281 ± 0.180	0.145 ± 0.007	2.669 ± 0.232	2.053 ± 0.269	1.071 ± 0.331
−2.50	−61.8 ± 8.1	126.2 ± 10.4	0.022 ± 0.054	0.049 ± 0.049	2.597 ± 0.168	0.143 ± 0.006	2.623 ± 0.218	1.696 ± 0.247	1.672 ± 0.305
−2.00	−45.9 ± 8.9	160.9 ± 12.1	0.056 ± 0.043	0.097 ± 0.097	2.884 ± 0.163	0.141 ± 0.006	2.565 ± 0.219	2.371 ± 0.239	2.188 ± 0.306
−1.50	−37.8 ± 7.0	145.8 ± 9.7	0.059 ± 0.038	0.074 ± 0.074	3.223 ± 0.147	0.148 ± 0.005	2.711 ± 0.199	2.567 ± 0.217	1.959 ± 0.272
−0.99	−16.8 ± 5.7	123.4 ± 8.1	0.007 ± 0.038	0.089 ± 0.089	3.229 ± 0.151	0.151 ± 0.005	2.802 ± 0.172	2.291 ± 0.199	2.022 ± 0.239
−0.49	5.7 ± 5.8	128.4 ± 8.4	0.016 ± 0.037	0.100 ± 0.100	3.124 ± 0.147	0.146 ± 0.005	2.051 ± 0.169	2.218 ± 0.191	2.328 ± 0.229
−0.11	27.4 ± 7.1	154.9 ± 9.2	−0.004 ± 0.038	0.004 ± 0.004	2.947 ± 0.174	0.154 ± 0.006	3.089 ± 0.201	2.650 ± 0.229	2.362 ± 0.285
0.14	21.6 ± 7.4	144.6 ± 9.9	−0.038 ± 0.042	0.054 ± 0.054	3.104 ± 0.176	0.167 ± 0.007	3.376 ± 0.195	2.363 ± 0.246	1.834 ± 0.282
0.51	29.8 ± 6.1	151.5 ± 7.2	−0.007 ± 0.035	−0.014 ± −0.014	3.334 ± 0.142	0.159 ± 0.005	2.985 ± 0.163	1.865 ± 0.202	2.285 ± 0.231
1.02	54.7 ± 6.2	149.6 ± 8.2	−0.052 ± 0.032	0.015 ± 0.015	3.244 ± 0.149	0.154 ± 0.006	2.795 ± 0.185	2.287 ± 0.215	1.744 ± 0.250
1.52	59.6 ± 7.0	148.3 ± 8.6	−0.022 ± 0.039	−0.015 ± −0.015	3.202 ± 0.158	0.136 ± 0.006	2.418 ± 0.196	1.956 ± 0.231	2.158 ± 0.267
2.03	86.8 ± 8.6	158.5 ± 9.8	−0.161 ± 0.038	−0.006 ± −0.006	2.579 ± 0.163	0.133 ± 0.007	2.531 ± 0.207	2.490 ± 0.241	2.063 ± 0.269
2.53	109.9 ± 8.6	137.6 ± 11.3	−0.025 ± 0.053	0.052 ± 0.052	2.577 ± 0.169	0.155 ± 0.008	3.107 ± 0.222	1.288 ± 0.264	1.927 ± 0.272
3.15	109.9 ± 8.3	156.8 ± 11.0	−0.079 ± 0.038	0.018 ± 0.018	3.477 ± 0.163	0.133 ± 0.007	2.443 ± 0.196	1.597 ± 0.273	2.392 ± 0.261
3.91	118.5 ± 9.8	106.9 ± 12.0	−0.004 ± 0.068	0.084 ± 0.084	4.359 ± 0.174	0.127 ± 0.008	2.249 ± 0.209	1.649 ± 0.282	1.163 ± 0.267
4.79	148.4 ± 8.7	133.8 ± 8.8	−0.017 ± 0.058	−0.071 ± −0.071	3.110 ± 0.170	0.119 ± 0.008	2.437 ± 0.206	1.556 ± 0.277	1.416 ± 0.267
5.91	162.7 ± 8.2	113.7 ± 11.5	−0.044 ± 0.051	0.036 ± 0.036	2.729 ± 0.179	0.122 ± 0.008	2.502 ± 0.216	1.288 ± 0.283	1.798 ± 0.292
7.29	188.4 ± 8.4	91.3 ± 11.4	−0.032 ± 0.068	0.036 ± 0.036	3.979 ± 0.204	0.132 ± 0.010	2.545 ± 0.252	1.390 ± 0.330	1.872 ± 0.341
9.16	188.1 ± 8.9	95.4 ± 13.0	−0.009 ± 0.055	0.016 ± 0.016	3.920 ± 0.195	0.133 ± 0.009	2.984 ± 0.266	2.035 ± 0.331	1.599 ± 0.336
12.01	203.6 ± 11.5	103.6 ± 14.6	−0.023 ± 0.084	0.085 ± 0.085	3.739 ± 0.210	0.137 ± 0.010	2.513 ± 0.309	1.509 ± 0.368	1.971 ± 0.378
17.99	194.7 ± 10.5	78.9 ± 19.9	−0.040 ± 0.061	0.005 ± 0.005	3.515 ± 0.258	0.104 ± 0.013	2.656 ± 0.374	2.391 ± 0.470	1.559 ± 0.466
UGC 4000									
−32.09	272.0 ± 54.9	120.4 ± 70.6	0.014 ± 0.263	−0.002 ± 0.324	1.772 ± 0.861	−0.005 ± 0.034	2.763 ± 0.957	−1.097 ± 1.459	3.065 ± 1.413
−16.86	234.1 ± 21.6	67.7 ± 20.8	−0.023 ± 0.241	0.022 ± 0.068	3.509 ± 0.355	0.099 ± 0.015	2.759 ± 0.433	0.013 ± 0.595	0.972 ± 0.604
−8.50	154.0 ± 12.3	109.9 ± 16.8	−0.068 ± 0.062	−0.004 ± 0.114	2.191 ± 0.348	0.144 ± 0.013	2.974 ± 0.415	2.408 ± 0.520	2.161 ± 0.536
−6.25	161.9 ± 10.3	105.0 ± 15.3	−0.046 ± 0.061	0.019 ± 0.101	2.067 ± 0.333	0.169 ± 0.012	3.495 ± 0.376	1.689 ± 0.438	0.967 ± 0.444
−4.89	122.3 ± 11.5	129.2 ± 14.7	−0.061 ± 0.054	−0.020 ± 0.085	1.249 ± 0.315	0.181 ± 0.011	3.720 ± 0.372	1.930 ± 0.437	2.475 ± 0.444
−4.02	132.4 ± 11.5	138.8 ± 15.5	−0.054 ± 0.058	0.038 ± 0.073	1.148 ± 0.284	0.188 ± 0.010	2.978 ± 0.379	3.105 ± 0.425	2.373 ± 0.453
−3.26	88.2 ± 9.8	160.8 ± 12.0	−0.059 ± 0.041	0.006 ± 0.056	0.394 ± 0.270	0.216 ± 0.009	3.340 ± 0.358	3.385 ± 0.370	3.115 ± 0.392
−2.64	71.6 ± 10.7	159.1 ± 11.7	0.032 ± 0.054	−0.012 ± 0.050	0.552 ± 0.292	0.216 ± 0.010	4.229 ± 0.379	2.255 ± 0.381	3.067 ± 0.426
−2.14	46.9 ± 10.2	165.2 ± 11.4	−0.055 ± 0.047	−0.050 ± 0.052	0.535 ± 0.258	0.225 ± 0.009	4.347 ± 0.365	2.365 ± 0.301	2.070 ± 0.385
−1.63	53.3 ± 10.0	175.9 ± 10.4	−0.046 ± 0.047	−0.051 ± 0.044	1.163 ± 0.227	0.204 ± 0.008	4.342 ± 0.333	2.655 ± 0.269	2.614 ± 0.347
−1.13	15.1 ± 8.6	157.0 ± 9.1	−0.014 ± 0.048	−0.031 ± 0.038	0.832 ± 0.227	0.225 ± 0.008	3.971 ± 0.321	2.465 ± 0.254	2.315 ± 0.343
−0.75	12.2 ± 10.4	143.9 ± 13.6	−0.034 ± 0.046	0.015 ± 0.070	0.892 ± 0.274	0.206 ± 0.009	3.324 ± 0.370	2.034 ± 0.293	1.563 ± 0.398
−0.50	−0.6 ± 9.5	162.6 ± 11.8	−0.013 ± 0.042	−0.020 ± 0.055	1.382 ± 0.284	0.238 ± 0.009	3.889 ± 0.382	2.275 ± 0.299	2.850 ± 0.415
−0.25	−17.0 ± 10.2	160.8 ± 12.8	−0.009 ± 0.042	0.013 ± 0.058	1.473 ± 0.279	0.251 ± 0.009	4.389 ± 0.371	1.822 ± 0.292	2.276 ± 0.412
0.00	−10.1 ± 10.3	159.1 ± 11.4	−0.029 ± 0.054	−0.029 ± 0.048	0.499 ± 0.283	0.200 ± 0.009	3.849 ± 0.381	1.931 ± 0.300	0.794 ± 0.418
0.26	−21.6 ± 10.1	141.4 ± 13.5	0.031 ± 0.047	0.008 ± 0.070	0.834 ± 0.291	0.199 ± 0.009	4.061 ± 0.386	2.628 ± 0.316	2.456 ± 0.387
0.51	−27.7 ± 10.4	147.8 ± 13.0	−0.013 ± 0.051	0.015 ± 0.059	1.503 ± 0.297	0.221 ± 0.010	4.618 ± 0.394	2.346 ± 0.334	2.700 ± 0.378
0.88	−24.3 ± 8.5	144.7 ± 10.9	−0.046 ± 0.041	0.017 ± 0.056	1.042 ± 0.237	0.208 ± 0.008	3.218 ± 0.302	2.850 ± 0.275	1.857 ± 0.313
1.39	−52.8 ± 8.8	136.5 ± 11.7	0.028 ± 0.048	−0.001 ± 0.061	1.074 ± 0.267	0.211 ± 0.008	3.528 ± 0.336	2.537 ± 0.307	2.079 ± 0.349
1.89	−50.1 ± 8.9	137.4 ± 11.5	0.024 ± 0.053	0.037 ± 0.052	1.562 ± 0.291	0.219 ± 0.009	4.722 ± 0.331	2.522 ± 0.332	2.457 ± 0.368
2.39	−92.8 ± 11.8	170.3 ± 13.1	0.037 ± 0.052	−0.030 ± 0.055	−0.366 ± 0.311	0.216 ± 0.009	3.250 ± 0.364	2.219 ± 0.366	2.032 ± 0.416
3.02	−102.5 ± 9.3	136.1 ± 12.3	0.080 ± 0.044	0.011 ± 0.067	0.515 ± 0.289	0.211 ± 0.008	3.197 ± 0.333	2.291 ± 0.366	3.226 ± 0.385
3.77	−91.8 ± 10.1	121.3 ± 14.2	−0.019 ± 0.051	0.009 ± 0.086	−0.188 ± 0.340	0.169 ± 0.010	3.006 ± 0.384	0.940 ± 0.420	0.922 ± 0.439
4.76	−134.9 ± 10.9	143.4 ± 14.0	0.093 ± 0.047	0.020 ± 0.073	0.680 ± 0.350	0.211 ± 0.010	3.425 ± 0.419	2.617 ± 0.415	2.378 ± 0.419
6.48	−171.2 ± 13.1	121.1 ± 13.1	0.026 ± 0.096	−0.063 ± 0.059	1.878 ± 0.407	0.154 ± 0.012	2.835 ± 0.460	3.216 ± 0.476	1.906 ± 0.470
9.64	−175.2 ± 14.9	84.2 ± 14.9	−0.008 ± 0.150	−0.012 ± 0.061	2.910 ± 0.413	0.153 ± 0.013	3.164 ± 0.500	0.565 ± 0.529	1.337 ± 0.478
14.18	−206.3 ± 26.9	41.1 ± 19.1	0.003 ± 0.493	−0.015 ± 0.140	3.129 ± 0.391	0.086 ± 0.012	2.144 ± 0.472	1.115 ± 0.461	0.669 ± 0.475
31.92	−185.8 ± 59.6	37.5 ± 195.9	0.005 ± 1.005	−0.003 ± 2.585	4.759 ± 0.811	0.077 ± 0.026	4.633 ± 1.111	−4.010 ± 1.181	−1.736 ± 1.121
UGC 4341									
−24.24	−202.7 ± 12.6	86.7 ± 15.7	−0.037 ± 0.114	0.027 ± 0.093	1.890 ± 0.440	0.132 ± 0.015	3.609 ± 0.543	2.501 ± 0.717	2.313 ± 0.520

Table A1 – *continued*

r (arcsec)	v (km s⁻¹)	σ (km s⁻¹)	h₃	h₄	Hβ (Å)	Mg₂ (mag)	Mg_b (Å)	Fe5270 (Å)	Fe5335 (Å)
(1)	(2)	(3)	(4)	(5)	(6)	(7)	(8)	(9)	(10)
−13.09	−190.5 ± 5.9	89.0 ± 8.3	0.030 ± 0.054	0.061 ± 0.055	2.336 ± 0.219	0.248 ± 0.008	4.805 ± 0.284	2.987 ± 0.353	2.879 ± 0.256
−9.73	−161.4 ± 5.8	106.1 ± 8.1	−0.020 ± 0.045	0.072 ± 0.045	1.064 ± 0.206	0.235 ± 0.007	4.034 ± 0.258	2.268 ± 0.299	2.453 ± 0.223
−7.04	−124.8 ± 5.9	106.6 ± 8.0	0.005 ± 0.045	0.062 ± 0.045	1.684 ± 0.203	0.235 ± 0.007	4.532 ± 0.264	1.713 ± 0.278	2.886 ± 0.218
−5.15	−104.2 ± 6.4	139.2 ± 8.8	−0.041 ± 0.038	0.063 ± 0.041	1.882 ± 0.192	0.247 ± 0.007	4.057 ± 0.266	2.599 ± 0.267	2.528 ± 0.206
−3.91	−89.5 ± 6.3	156.3 ± 8.2	−0.020 ± 0.033	0.035 ± 0.035	1.578 ± 0.178	0.257 ± 0.007	4.334 ± 0.256	2.743 ± 0.252	2.615 ± 0.201
−3.04	−88.4 ± 6.5	183.5 ± 8.3	−0.036 ± 0.029	0.022 ± 0.032	1.340 ± 0.166	0.261 ± 0.006	4.284 ± 0.240	2.380 ± 0.235	2.709 ± 0.192
−2.42	−80.8 ± 6.8	184.2 ± 8.7	−0.029 ± 0.031	0.055 ± 0.031	1.644 ± 0.169	0.257 ± 0.006	4.049 ± 0.243	2.302 ± 0.235	3.095 ± 0.195
−1.91	−80.1 ± 5.6	160.7 ± 7.9	−0.001 ± 0.030	0.087 ± 0.032	2.310 ± 0.146	0.259 ± 0.005	4.397 ± 0.204	2.361 ± 0.195	2.101 ± 0.163
−1.41	−61.7 ± 5.2	192.5 ± 6.2	0.013 ± 0.023	−0.001 ± 0.024	2.017 ± 0.132	0.260 ± 0.005	4.439 ± 0.185	2.945 ± 0.172	2.343 ± 0.147
−1.04	−37.4 ± 6.3	187.6 ± 8.3	0.000 ± 0.029	0.067 ± 0.029	1.605 ± 0.165	0.253 ± 0.005	4.267 ± 0.219	2.202 ± 0.200	2.115 ± 0.178
−0.79	−30.1 ± 5.9	209.1 ± 7.9	−0.044 ± 0.023	0.090 ± 0.026	2.007 ± 0.151	0.270 ± 0.005	4.379 ± 0.200	2.897 ± 0.174	3.016 ± 0.162
−0.53	−17.6 ± 5.5	185.9 ± 7.6	−0.014 ± 0.025	0.091 ± 0.027	1.934 ± 0.158	0.269 ± 0.005	4.324 ± 0.193	3.345 ± 0.170	2.436 ± 0.156
−0.28	0.5 ± 6.1	206.4 ± 7.9	0.035 ± 0.025	0.051 ± 0.027	1.028 ± 0.172	0.261 ± 0.005	4.875 ± 0.206	2.914 ± 0.171	2.613 ± 0.173
−0.03	1.7 ± 5.7	205.7 ± 7.0	0.003 ± 0.024	0.034 ± 0.024	2.522 ± 0.172	0.264 ± 0.005	4.816 ± 0.200	2.543 ± 0.165	3.202 ± 0.173
0.22	2.7 ± 6.3	194.1 ± 8.7	−0.041 ± 0.027	0.094 ± 0.029	1.229 ± 0.193	0.265 ± 0.006	4.493 ± 0.220	2.681 ± 0.183	2.499 ± 0.185
0.59	40.3 ± 5.1	204.5 ± 6.6	−0.035 ± 0.021	0.051 ± 0.023	0.730 ± 0.173	0.278 ± 0.005	4.486 ± 0.186	3.064 ± 0.143	2.406 ± 0.162
1.10	69.4 ± 6.0	200.4 ± 8.0	−0.033 ± 0.025	0.071 ± 0.027	1.545 ± 0.202	0.279 ± 0.006	4.492 ± 0.215	2.800 ± 0.157	2.646 ± 0.190
1.60	85.0 ± 6.6	183.4 ± 9.0	−0.021 ± 0.031	0.074 ± 0.031	1.170 ± 0.228	0.264 ± 0.006	4.302 ± 0.245	2.274 ± 0.175	2.927 ± 0.212
2.22	110.7 ± 6.2	186.6 ± 7.7	−0.020 ± 0.027	0.007 ± 0.031	1.289 ± 0.210	0.266 ± 0.006	4.391 ± 0.230	2.922 ± 0.176	2.910 ± 0.217
3.10	106.5 ± 6.1	153.8 ± 8.1	−0.028 ± 0.033	0.047 ± 0.034	1.678 ± 0.195	0.245 ± 0.006	4.010 ± 0.219	3.048 ± 0.173	2.901 ± 0.220
4.33	104.6 ± 5.8	148.7 ± 7.3	−0.009 ± 0.032	−0.001 ± 0.034	1.583 ± 0.205	0.249 ± 0.006	4.233 ± 0.231	2.967 ± 0.170	2.533 ± 0.224
6.32	131.1 ± 6.3	121.8 ± 8.4	0.009 ± 0.043	0.063 ± 0.041	1.353 ± 0.215	0.232 ± 0.007	4.065 ± 0.238	2.637 ± 0.174	2.783 ± 0.236
9.27	182.5 ± 5.5	87.3 ± 7.8	−0.035 ± 0.048	0.035 ± 0.058	1.262 ± 0.226	0.245 ± 0.008	4.520 ± 0.259	2.552 ± 0.190	2.969 ± 0.254
13.30	207.5 ± 6.1	84.1 ± 8.0	0.004 ± 0.059	0.050 ± 0.053	1.098 ± 0.251	0.243 ± 0.008	4.328 ± 0.272	2.881 ± 0.202	2.135 ± 0.277
25.48	226.4 ± 18.7	59.9 ± 24.1	0.014 ± 0.238	−0.006 ± 0.211	0.363 ± 0.600	0.164 ± 0.020	2.429 ± 0.666	3.979 ± 0.520	2.646 ± 0.731

UGC 5026

r (arcsec)	v (km s⁻¹)	σ (km s⁻¹)	h₃	h₄	Hβ (Å)	Mg₂ (mag)	Mg_b (Å)	Fe5270 (Å)	Fe5335 (Å)
−22.40	79.6 ± 24.1	179.9 ± 27.1	–	–	1.285 ± 0.429	0.015 ± 0.013	1.465 ± 0.479	0.986 ± 0.548	0.677 ± 0.796
−10.06	119.2 ± 7.7	166.6 ± 9.0	–	–	2.048 ± 0.161	0.117 ± 0.005	2.116 ± 0.200	1.425 ± 0.216	1.440 ± 0.300
−7.08	110.5 ± 6.8	168.9 ± 7.6	–	–	1.763 ± 0.129	0.108 ± 0.005	2.240 ± 0.165	1.957 ± 0.185	1.477 ± 0.253
−5.34	95.2 ± 5.4	151.8 ± 6.5	–	–	2.420 ± 0.125	0.124 ± 0.004	2.283 ± 0.157	2.315 ± 0.179	1.939 ± 0.216
−3.98	75.9 ± 4.5	162.3 ± 5.1	–	–	2.051 ± 0.128	0.157 ± 0.004	2.971 ± 0.153	2.291 ± 0.169	2.295 ± 0.200
−2.70	67.1 ± 3.4	130.0 ± 4.3	–	–	2.495 ± 0.123	0.168 ± 0.004	2.967 ± 0.151	2.453 ± 0.164	1.935 ± 0.183
−1.68	31.7 ± 3.2	126.1 ± 3.9	–	–	2.367 ± 0.135	0.188 ± 0.005	3.400 ± 0.147	2.668 ± 0.161	2.490 ± 0.176
−1.06	17.0 ± 2.5	125.6 ± 3.2	–	–	2.067 ± 0.118	0.196 ± 0.004	3.498 ± 0.127	2.517 ± 0.138	2.509 ± 0.147
−0.70	7.0 ± 2.7	124.3 ± 3.3	–	–	2.304 ± 0.123	0.197 ± 0.004	3.435 ± 0.132	2.776 ± 0.149	2.539 ± 0.158
−0.45	4.9 ± 2.6	126.8 ± 3.2	–	–	2.311 ± 0.122	0.205 ± 0.004	3.613 ± 0.135	2.805 ± 0.144	2.644 ± 0.145
−0.20	4.2 ± 2.4	121.9 ± 3.1	–	–	2.195 ± 0.121	0.208 ± 0.004	3.677 ± 0.140	2.763 ± 0.138	2.453 ± 0.141
0.05	−4.8 ± 2.3	126.3 ± 3.0	–	–	2.487 ± 0.114	0.202 ± 0.004	3.538 ± 0.132	2.709 ± 0.133	2.551 ± 0.137
0.30	−8.5 ± 2.3	117.1 ± 2.9	–	–	2.385 ± 0.111	0.208 ± 0.004	3.638 ± 0.125	2.861 ± 0.132	2.525 ± 0.144
0.67	−12.3 ± 2.1	116.4 ± 2.7	–	–	2.378 ± 0.097	0.196 ± 0.004	3.219 ± 0.116	2.460 ± 0.118	2.652 ± 0.128
1.18	−24.6 ± 2.5	117.5 ± 3.2	–	–	2.594 ± 0.110	0.192 ± 0.004	3.455 ± 0.134	2.734 ± 0.137	2.128 ± 0.149
1.69	−37.1 ± 3.2	115.3 ± 3.6	–	–	2.951 ± 0.118	0.185 ± 0.005	2.934 ± 0.146	2.809 ± 0.144	2.523 ± 0.164
2.31	−56.6 ± 2.6	111.8 ± 3.4	–	–	2.684 ± 0.109	0.176 ± 0.004	2.977 ± 0.131	2.710 ± 0.133	2.505 ± 0.152
3.06	−71.5 ± 3.4	122.2 ± 4.1	–	–	2.375 ± 0.129	0.177 ± 0.005	3.218 ± 0.155	2.450 ± 0.156	2.071 ± 0.181
3.93	−78.8 ± 4.0	130.9 ± 4.8	–	–	2.651 ± 0.141	0.159 ± 0.005	2.925 ± 0.163	2.249 ± 0.167	2.217 ± 0.193
5.17	−73.9 ± 5.5	152.2 ± 6.4	–	–	2.686 ± 0.155	0.131 ± 0.006	2.162 ± 0.184	2.141 ± 0.191	1.987 ± 0.222
7.02	−52.1 ± 7.1	178.6 ± 8.2	–	–	1.889 ± 0.157	0.125 ± 0.005	2.696 ± 0.195	1.903 ± 0.207	1.903 ± 0.241
10.84	−95.3 ± 5.9	120.2 ± 7.4	–	–	1.561 ± 0.199	0.147 ± 0.007	2.392 ± 0.238	1.665 ± 0.253	1.999 ± 0.284
24.72	−95.7 ± 21.2	99.5 ± 27.0	–	–	1.743 ± 0.592	0.087 ± 0.022	0.795 ± 0.719	−1.230 ± 0.791	1.657 ± 0.907

UGC 5184

| r (arcsec)	v (km s⁻¹)	σ (km s⁻¹)	h₃	h₄	Hβ (Å)	Mg₂ (mag)	Mg_b (Å)	Fe5270 (Å)	Fe5335 (Å)
−25.17	−275.1 ± 49.5	282.2 ± 53.0	−0.052 ± 0.100	0.027 ± 0.111	1.748 ± 0.877	0.092 ± 0.029	2.946 ± 1.073	6.592 ± 1.105	4.146 ± 1.406
−9.80	−130.0 ± 6.1	66.3 ± 12.3	0.061 ± 0.059	0.020 ± 0.127	2.873 ± 0.321	0.159 ± 0.011	3.323 ± 0.353	3.006 ± 0.375	3.173 ± 0.303
−5.06	−85.3 ± 6.6	97.6 ± 7.0	−0.047 ± 0.055	−0.063 ± 0.050	1.900 ± 0.274	0.188 ± 0.009	3.285 ± 0.308	2.713 ± 0.329	2.775 ± 0.226
−3.13	−74.5 ± 7.4	106.6 ± 9.7	0.020 ± 0.055	0.028 ± 0.055	1.330 ± 0.283	0.201 ± 0.009	3.040 ± 0.314	2.386 ± 0.333	1.627 ± 0.227
−1.88	−71.8 ± 6.2	95.4 ± 9.2	0.044 ± 0.046	0.019 ± 0.068	0.482 ± 0.300	0.159 ± 0.009	2.927 ± 0.305	2.267 ± 0.320	2.580 ± 0.222
−1.00	−38.4 ± 6.1	114.5 ± 8.7	0.110 ± 0.039	0.103 ± 0.051	1.184 ± 0.301	0.162 ± 0.008	2.245 ± 0.280	2.460 ± 0.285	1.682 ± 0.197
−0.38	−14.8 ± 6.4	130.5 ± 8.2	0.130 ± 0.035	0.032 ± 0.046	0.918 ± 0.278	0.141 ± 0.007	2.497 ± 0.246	2.385 ± 0.256	1.238 ± 0.176
−0.01	−6.0 ± 7.7	147.4 ± 10.2	0.100 ± 0.038	0.061 ± 0.048	1.563 ± 0.266	0.120 ± 0.007	3.177 ± 0.256	2.053 ± 0.274	1.382 ± 0.197
0.24	5.5 ± 7.7	135.0 ± 10.6	0.016 ± 0.047	0.091 ± 0.044	2.876 ± 0.229	0.125 ± 0.007	3.121 ± 0.240	2.376 ± 0.265	1.832 ± 0.196
0.46	24.7 ± 7.8	123.9 ± 10.2	−0.004 ± 0.051	0.035 ± 0.047	3.078 ± 0.213	0.122 ± 0.007	2.462 ± 0.238	2.388 ± 0.270	1.391 ± 0.201
0.74	30.3 ± 7.3	121.3 ± 9.8	0.022 ± 0.041	0.003 ± 0.058	2.439 ± 0.201	0.127 ± 0.007	2.310 ± 0.244	1.681 ± 0.289	1.320 ± 0.198
1.11	41.2 ± 7.6	130.9 ± 8.4	−0.023 ± 0.049	−0.022 ± 0.041	2.950 ± 0.180	0.138 ± 0.007	3.215 ± 0.222	1.341 ± 0.257	2.041 ± 0.188
1.61	41.3 ± 7.4	127.7 ± 9.6	−0.053 ± 0.041	−0.017 ± 0.055	2.166 ± 0.220	0.172 ± 0.007	3.452 ± 0.267	1.809 ± 0.312	1.504 ± 0.223
2.24	57.6 ± 6.0	109.0 ± 7.5	−0.051 ± 0.041	−0.029 ± 0.051	2.016 ± 0.206	0.185 ± 0.007	3.259 ± 0.245	2.305 ± 0.280	2.209 ± 0.207
3.12	63.0 ± 6.2	106.7 ± 8.7	−0.006 ± 0.047	0.079 ± 0.046	1.814 ± 0.216	0.192 ± 0.008	3.891 ± 0.259	3.139 ± 0.287	2.799 ± 0.211
4.24	73.1 ± 6.6	108.4 ± 8.5	−0.001 ± 0.045	−0.008 ± 0.055	2.049 ± 0.239	0.198 ± 0.008	3.211 ± 0.301	3.350 ± 0.324	2.465 ± 0.247
5.74	90.4 ± 7.4	117.9 ± 8.1	−0.026 ± 0.050	−0.035 ± 0.046	1.791 ± 0.244	0.193 ± 0.008	3.151 ± 0.308	2.984 ± 0.326	2.721 ± 0.274
8.17	130.1 ± 7.2	92.1 ± 10.2	−0.062 ± 0.048	0.005 ± 0.084	2.683 ± 0.266	0.191 ± 0.010	3.122 ± 0.333	2.510 ± 0.368	3.241 ± 0.312
20.79	138.8 ± 26.1	72.0 ± 24.6	0.006 ± 0.292	−0.005 ± 0.070	1.649 ± 0.602	0.175 ± 0.024	1.781 ± 0.780	2.524 ± 0.944	−0.218 ± 0.825
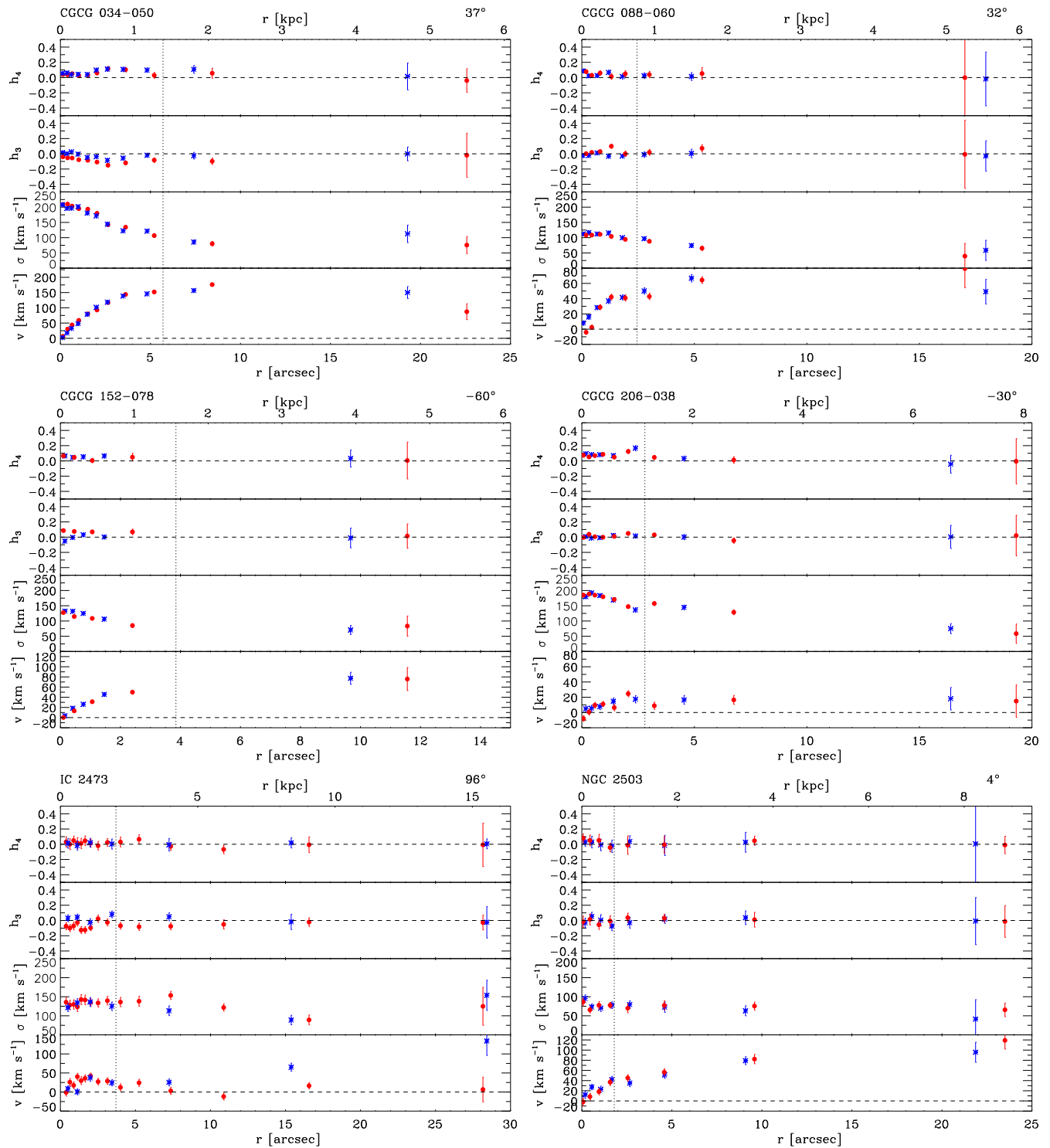
Figure A2. Stellar kinematics measured along the major axis of the sample galaxies. For each axis, the curves are folded around the nucleus. Blue asterisks and red circles refer to the data measured along the approaching and residing sides of the galaxy, respectively. The radial profiles of the LOS velocity (v) after the subtraction of the systemic velocity, the velocity dispersion (σ), the third- and fourth-order coefficients of the Gauss–Hermite decomposition of the LOSVD (h_3 and h_4) are shown (panels from top to bottom). The vertical dashed line corresponds to the radius r_{bd}, where the surface brightness contribution of the bulge is equal to that of the remaining components.
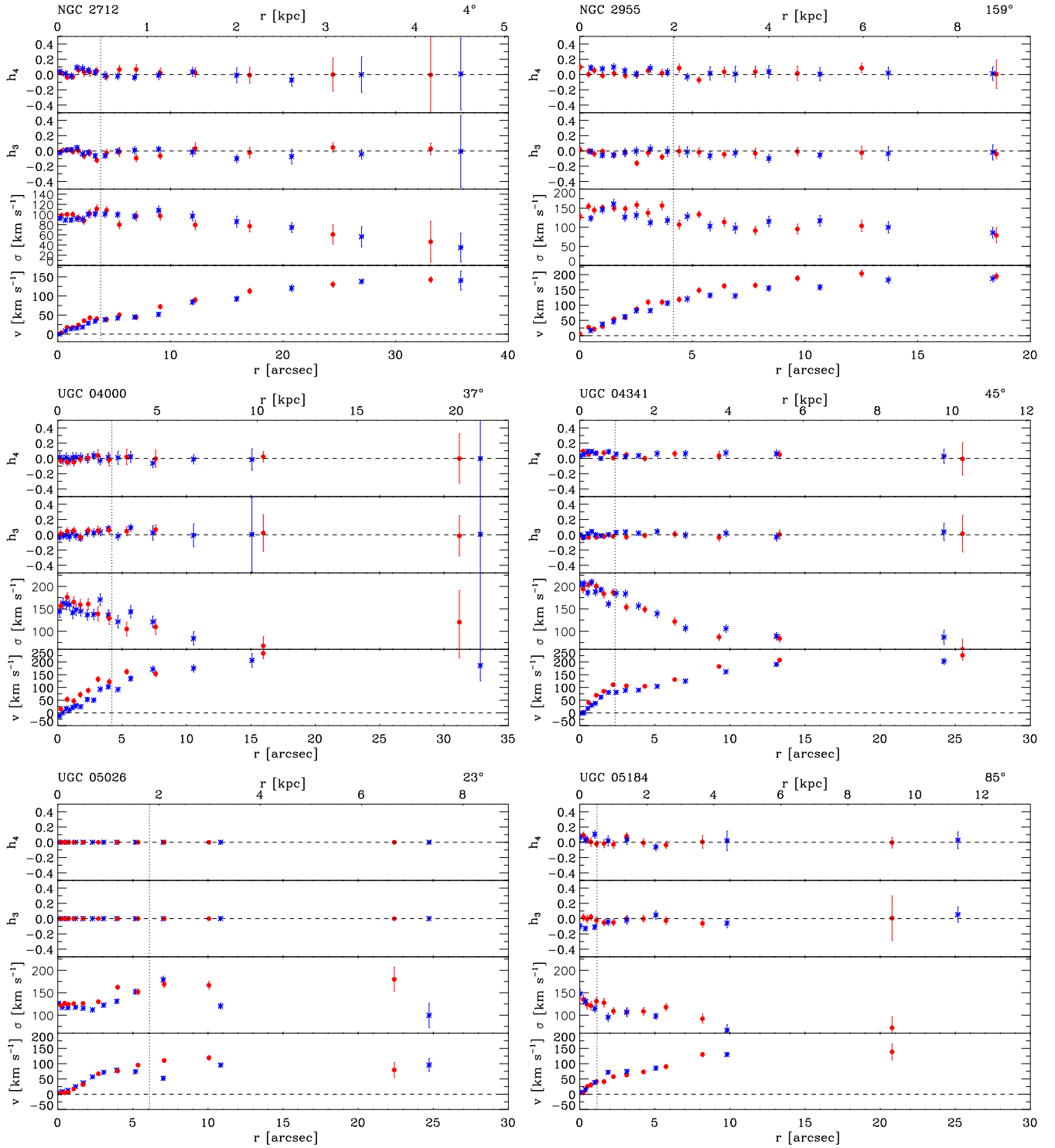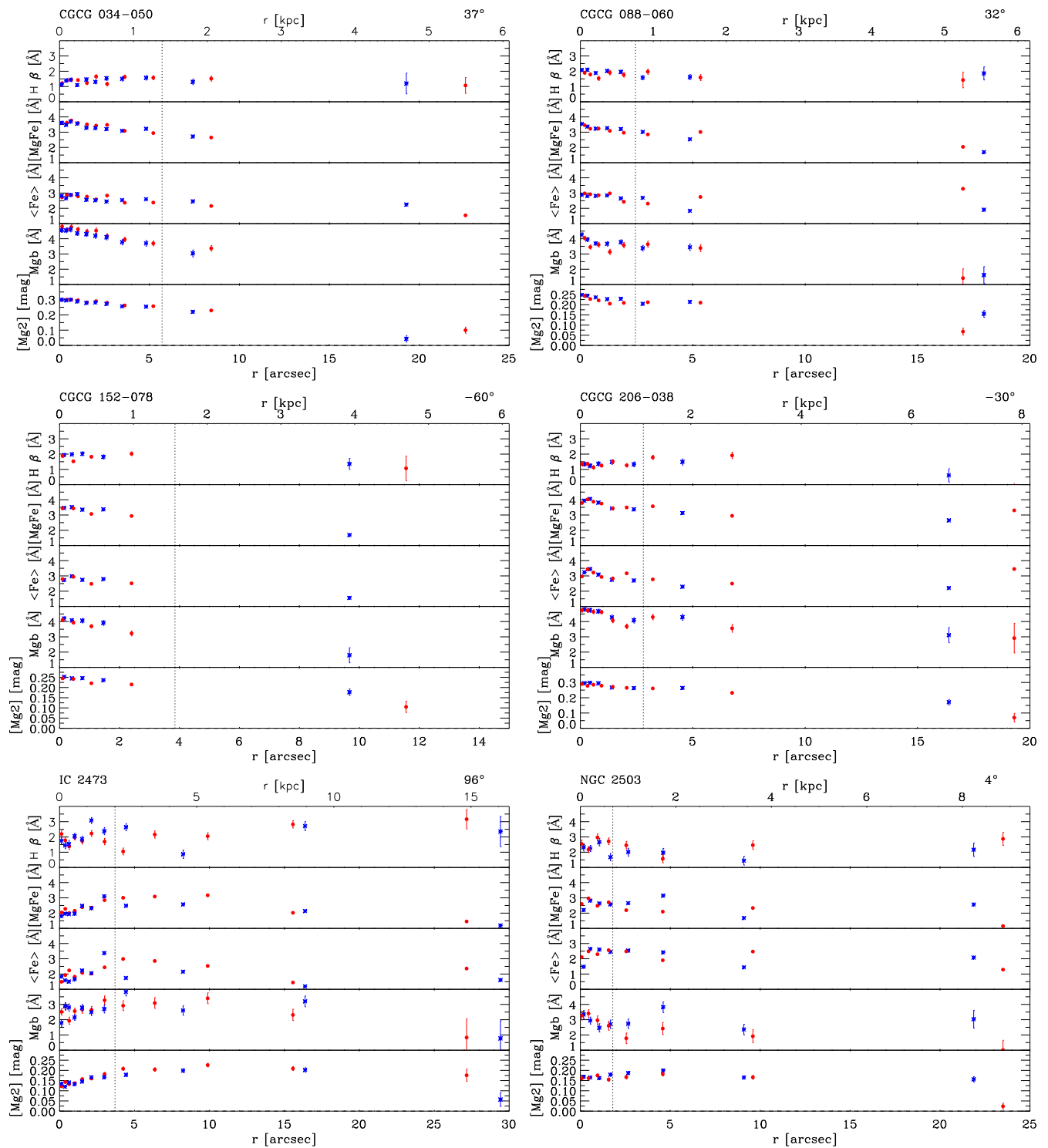
Figure A2 *– continued*

Figure A3. Line-strength indices measured along the major axis of the sample galaxies. For each axis, the curves are folded around the nucleus. Blue asterisks and red circles refer to the data measured along the approaching and residing side of the galaxy, respectively. The radial profiles of the line-strength indices Hβ, [MgFe]′, ⟨Fe⟩, Mg$_b$, and Mg$_2$ are shown (from top to bottom panel). The vertical dashed line corresponds to the radius r_{bd}, where the bulge contributes half of galaxy surface brightness. The name of the galaxy and position angle of the slit are given for each data set.
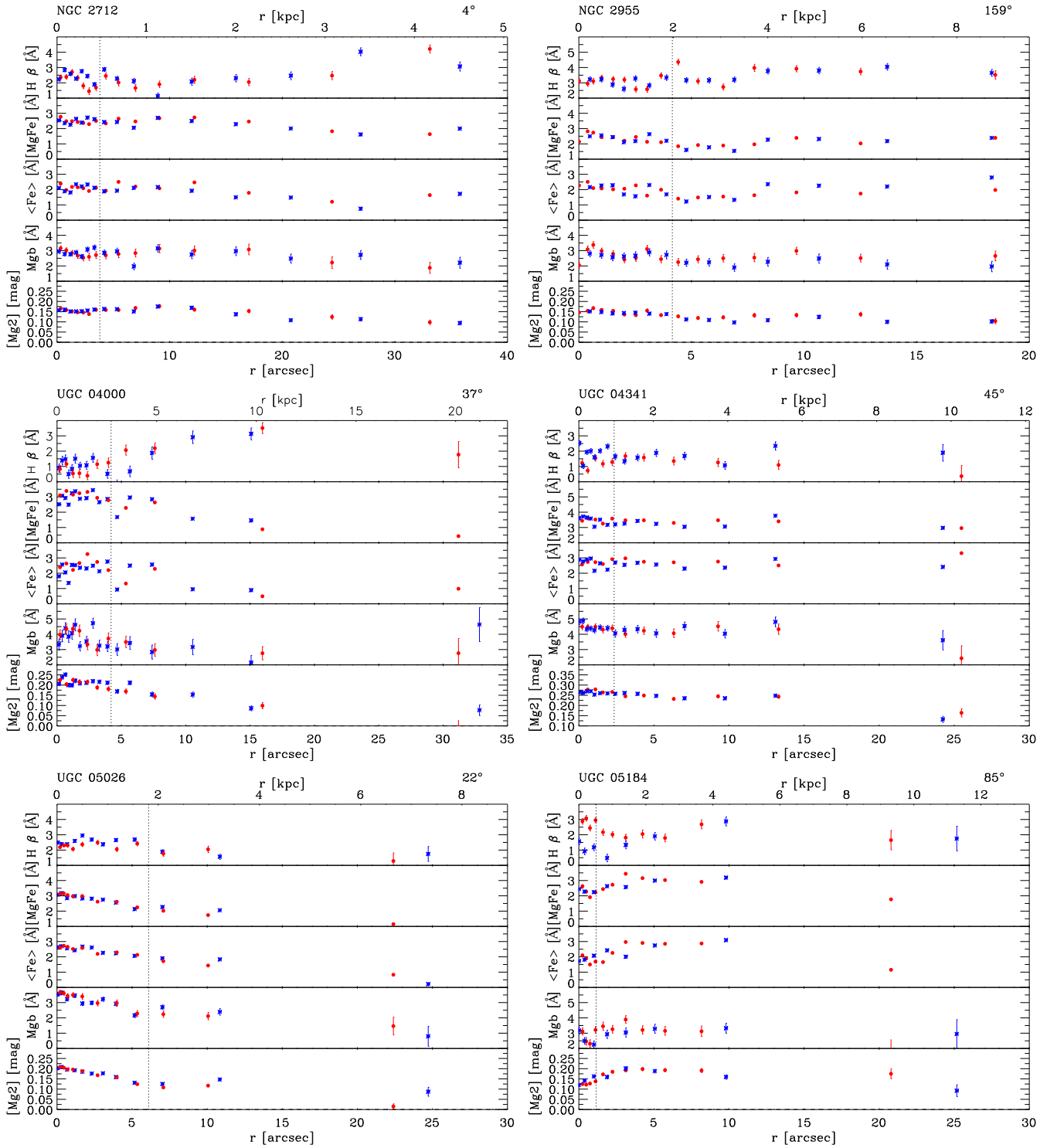
Figure A3 – *continued*

This paper has been typeset from a TEX/LATEX file prepared by the author.